ELECTROCHEMICAL IMPEDANCE SPECTROSCOPY ANALYSIS AND MODELING OF LITHIUM COBALT OXIDE/CARBON BATTERIES

By

SALIM EROL

A DISSERTATION PRESENTED TO THE GRADUATE SCHOOL
OF THE UNIVERSITY OF FLORIDA IN PARTIAL FULFILLMENT
OF THE REQUIREMENTS FOR THE DEGREE OF
DOCTOR OF PHILOSOPHY

UNIVERSITY OF FLORIDA

2015

To my parents, my sister, and her lovely son, Bulut

ACKNOWLEDGMENTS

First of all, I would like to express my special thanks of gratitude to Prof. Dr. Mark E. Orazem for guiding me in my dissertation with his large knowledge and experiences in electrochemical engineering field. He always has been very positive and patient during my studentship and research. I would like to thank Professors Kevin S. Jones, Jason E. Butler, Peng Jiang, Anuj Chauhan, and Kirk J. Ziegler, who have been my PhD committee members, for their extraordinary support and recommendations in this thesis process.I also thank to my research group members, who helped and supported me all the time.

TABLE OF CONTENTS

page

ACKNOWLEDGMENTS 4

LIST OF TABLES 7

LIST OF FIGURES 8

ABSTRACT 11

CHAPTER

1 INTRODUCTION 13

2 LITHIUM-ION BATTERIES 16

2.1 Negative Electrode (Anode) 19
2.2 Positive Electrode (Cathode) 19
2.3 Electrolyte 20

3 ELECTROCHEMICAL IMPEDANCE SPECTROSCOPY 22

4 EXPERIMENTAL METHOD 25

4.1 Materials 25
4.2 Instrumentation 25
4.3 Protocol 26

5 RESULTS AND DISCUSSION 29

5.1 State-of-Charge 29
5.2 Overcharge 29
5.3 Over-Discharge 35
5.4 Temperature 41

6 MATHEMATICAL MODELING 47

6.1 Measurement Model Analysis 47
6.1.1 Measurement Model 47
6.1.2 Measurement Model Results 48
6.2 Process Model Development 51
6.2.1 Anode 54
6.2.1.1 Cycling and SEI formation 54
6.2.1.2 Linear diffusion in anode 55
6.2.2 Electrolyte and Separator 56
6.2.3 Cathode 56
6.2.3.1 Anomalous diffusion in cathode 56
6.2.4 Process Model Results 57

7 CONCLUSIONS 69
REFERENCES 73
BIOGRAPHICAL SKETCH 78

LIST OF TABLES

Table page

6-1 Regression results for cell potential ranging from 4.2 to 3.8 V. 60

6-2 Regression results for cell potential ranging from 3.6 to 3.2 V. 60

6-3 Regression results for cell temperature ranging from 10 to 20 °C. 61

6-4 Regression results for cell temperature ranging from 30 to 50 °C. 62

LIST OF FIGURES

Figure page

2-1 Diagram comparing the rechargeable battery technologies as a function of volumetric and specific energy densities . . . 17

2-2 Schematic of the general structure and components of a Li-ion battery. . . . 18

3-1 Polarization curve and representation of impedance. . . . 23

3-2 A schematic representation of a Randles circuit. . . . 23

3-3 The simulation of an impedance spectrum in Nyquist format for the Randles circuit. . . . 24

4-1 The photograph of the LIR2032 coin cell. . . . 26

5-1 Impedance response in Nyquist format for a $LiCoO_2$|C coin cell under normal operating conditions with cell potential as a parameter. . . . 30

5-2 Impedance response in Nyquist format for a $LiCoO_2$|C coin cell under overcharge conditions with cell potential ranging from 4.20 to 4.60 V. . . . 31

5-3 Impedance response in Nyquist format for a $LiCoO_2$|C coin cell under overcharge conditions with cell potential ranging from 4.60 to 4.76 V. . . . 32

5-4 Impedance response in Nyquist format for a $LiCoO_2$|C coin cell under overcharge conditions with cell potential ranging from 4.76 to 5.00 V. . . . 33

5-5 Open-circuit potential as a function of time for an overcharged $LiCoO_2$|C coin cell. . . . 33

5-6 Impedance response in Nyquist format for a $LiCoO_2$|C coin cell during self-discharge under overcharge conditions with elapsed time as a parameter. . . . 34

5-7 Impedance response of a $LiCoO_2$|C coin cell at a potential of 4 V before and after the cell was overcharged. . . . 34

5-8 Discharge and charge capacity of a $LiCoO_2$|C coin cell before and after the cell was overcharged. . . . 35

5-9 Impedance response in Nyquist format for a $LiCoO_2$|C coin cell under over-discharge conditions with cell potential, ranging from 3.00 to 2.84 V. . . . 36

5-10 Impedance response in Nyquist format for a $LiCoO_2$|C coin cell under over-discharge conditions with cell potential ranging from 2.84 to 2.20 V. . . . 37

5-11 Open-circuit potential as a function of time for an over-discharged $LiCoO_2$|C coin cell. . . . 37

5-12 Impedance response in Nyquist format for a $LiCoO_2$|C coin cell during self-charge under over-discharge conditions with elapsed time as a parameter. 38

5-13 Impedance response of a $LiCoO_2$|C coin cell at a potential of 4 V before and after the cell was over-discharged. 39

5-14 Discharge and charge capacity of a $LiCoO_2$|C coin cell before and after the cell was over-discharged. 39

5-15 SEM micrographs of the $LiCoO_2$ cathode of a coin cell. 40

5-16 SEM micrographs of the carbon anode of a coin cell. 42

5-17 Impedance response in Nyquist format for a $LiCoO_2$|C coin cell under 4 V cell potential with the temperature, ranging from 20 to 60 °C, as a parameter. . . . 43

5-18 Discharge capacity of a $LiCoO_2$|C coin cell with the temperature ranging from 20 to 60 °C 44

5-19 Impedance response in Nyquist format for a $LiCoO_2$|C coin cell under 4 V cell potential with the temperature, ranging from 20 to -20 °C, as a parameter. . . . 45

5-20 Discharge capacity of a $LiCoO_2$|C coin cell with the temperature ranging from 20 to -20 °C 46

6-1 A schematic representation of the measurement model. 47

6-2 Scaled impedance result of a $LiCoO_2$|C cell at 4 V; A) before and after the cell was overcharged and B) before and after the cell was over-discharged. 50

6-3 Equivalent circuit model for Li-ion batteries designed by Osaka et al. 51

6-4 Equivalent circuit model for Li-ion batteries developed by Li et al. 52

6-5 Equivalent circuit model for Li-ion batteries designed by Gomez et al. 52

6-6 Equivalent circuit model for Li-ion batteries designed by Greenleaf et al. 53

6-7 Typical impedance response of a $LiCoO_2$|C coin cell at a potential of 3.6 V . . . 53

6-8 SEI formation during electrochemical cycling. 55

6-9 Equivalent circuit representation of the model developed in the present work for the complete Li-ion battery system. 58

6-10 Impedance response a $LiCoO_2$|C coin cell with cell potential as a parameter and fit 59

6-11 Impedance response a $LiCoO_2$|C coin cell with cell temperature as a parameter ranging from 10 to 50 °C and fit. 61

6-12 Regressed value of the anodic-SEI capacitance as a function of potential and temperature. 62

6-13 Regressed value of the anodic Warburg impedance coefficient as a function of potential and temperature. 63

6-14 Regressed value of the anodic charge-transfer resistance as a function of potential and temperature. 64

6-15 Regressed value of the SEI charge-transfer resistance as a function of potential and temperature. 64

6-16 Regressed value of the ohmic resistance as a function of potential and temperature. 65

6-17 Regressed value of the cathodic charge-transfer resistance as a function of potential and temperature. 65

6-18 Regressed value of the cathodic CPE exponent as a function of potential and temperature. 66

6-19 Regressed value of the cathodic CPE coefficient as a function of potential and temperature. 67

6-20 Regressed value of the cathodic anomalous diffusion exponent as a function of potential and temperature. 67

6-21 Regressed value of the cathodic anomalous diffusion lumped parameter as a function of potential and temperature. 68

Abstract of Dissertation Presented to the Graduate School
of the University of Florida in Partial Fulfillment of the
Requirements for the Degree of Doctor of Philosophy

ELECTROCHEMICAL IMPEDANCE SPECTROSCOPY ANALYSIS AND MODELING OF LITHIUM COBALT OXIDE/CARBON BATTERIES

By

Salim Erol

May 2015

Chair: Mark E. Orazem
Major: Chemical Engineering

This work provides the results of impedance measurements on commercially available $LiCoO_2$|C coin-type battery cells and a process model development with respect to these data. The impedance response was shown to be extremely sensitive to state-of-charge, overcharge, over-discharge, and surrounding temperature. The impedance showed a persistent change to the electrochemical characteristics of a coin cell subject to overcharge; whereas, the electrochemical characteristics returned to normal for a coin cell subject to over-discharge. A measurement model analysis was used to show the reversibility of the impedance behavior of an over-discharged cell and the irreversibility of the impedance response of an overcharged cell. A process model was developed to explain and interpret electrochemical reactions and mass transfer occurring in this type of broadly used Lithium-ion batteries. The process model revealed that the impedance result gives useful and unique information about the Li-ion battery dynamics.

The process model for impedance analysis was developed in the context of reactions and transport processes that were hypothesized to govern the performance of the battery. At the carbon electrode, lithium ions and solvent were considered to react to form a solid-electrolyte interphase (SEI). In addition, lithium ions were assumed to diffuse through the SEI to intercalate into the graphene layers. As these two processes involve an addition of currents, the corresponding impedances must be considered to be in parallel. Anomalous diffusion of lithium ions was invoked at the $LiCoO_2$ electrode to

account for the low-frequency line that was steeper than the 45 degrees predicted by ordinary diffusion. The inductive behavior on the impedance at very high frequencies was attributed to an artifact of the battery system with the help of the Kramers-Kronig relations. This model was fit to all impedance data collected. The model provided a good description for impedance of batteries under normal operating potentials and temperatures. The contribution of anomalous diffusion was diminished at elevated temperatures, suggesting that the free-energy well associated with anomalous or sticky diffusion was shallow.

CHAPTER 1
INTRODUCTION

Lithium-ion (Li-ion) batteries are rechargeable batteries that are frequently used as power sources for household and industrial applications because they have a higher energy and power density as compared to other batteries such as nickel-cadmium and lead-acid. The most common Li-ion batteries use a $LiCoO_2$ cathode, a graphite anode, and a non-aqueous electrolyte composed of lithium salt such as $LiPF_6$ in a mixture of organic solvents such as ethylene carbonate (EC), propylene carbonate (PC), dimethyl carbonate (DMC), and diethyl carbonate (DEC) [1, 2].

The cycle life and capacity of a Li-ion battery are reduced if it is overcharged or in some cases over-discharged. Kise et al. [3] measured the impedance at different temperatures of a Li-ion cell under its normal range of potential and tested the internal temperature of an overcharged cell. They did not indicate impedance growth while overcharging the battery. Li et al. [4] used impedance to compare cycling effects between uncoated $LiCoO_2$ and $FePO_4$-coated $LiCoO_2$ cathode materials. They showed temperature profiles while overcharging these batteries and mentioned thermal runaway for the uncoated $LiCoO_2$ cathode. Maleki and Howard [5] reported that over-discharging of Li-ion cells below 1.5 V may cause capacity losses and/or thermal stability changes which could impact tolerance to abuse conditions. They reported impedance diagrams which showed increases in high and low frequency asymptotes with cycle life. Chen et al. [6] determined the conductivity of a lithium secondary battery for different state-of-charge conditions using impedance spectroscopy. They added an aromatic monomer that is electropolymerized during overcharging the battery to the electrolyte. The insulating polymer film protected the battery from overcharging. Belov and Yang [7] used electrical impedance spectroscopy and scanning electron microscopy to characterize electrode materials at different state-of-overcharge conditions. A dramatic increase in resistance for the 4.6 and 5.0 V test was reported, but the interpretation was qualitative. Love and

Swider-Lyons [8] used the impedance spectroscopy technique to diagnose overcharged $LiCoO_2$|C prismatic cells. They measured impedances while gradually overcharging and discharging the battery. They showed that a single 4.6 V overcharge shows clear differentiation in the impedance values at 500 Hz, and proposed that a single-frequency impedance measurement at 500 Hz provides a simple means of monitoring battery health.

The availability of an accurate mathematical model of li-ion battery impedance is important in energy storage and electrochemistry fields. Such a model could be used to enable lifetime prediction from short-term tests, to design accelerated aging protocols, to inform reliability assessments, and to guide efforts to reduce degradation through materials design and system optimization. In order to reach these goals by rational design, it is essential for the model to be based on the underlying physics of degradation, rather than the simple fitting of empirical circuit models. Many earlier battery impedance models were developed as equivalent circuits [9–17] or by using charge and diffusion within single particles [18–20]. Osaka et al. [9] used a model with different time constants for diffusion to particles of different sizes in cathode. Greenleaf et al. [12] showed that the $LiFePO_4$ system yields a slope of 45 degrees at low frequency, which is consisted with ordinary diffusion impedance; whereas, the slope of their low frequency impedance data was steeper than 45 degrees for $LiCoO_2$ system. Gomez et al. [11] proposed an equivalent circuit model with an inductance, a bunch of R-C units, and an intercalation capacitance in series, so did Greenleaf et al. [12]. Li et al. [10] developed an electrochemistry-based impedance model for Li-ion batteries. Their model has an inductor, separate CPE elements for the anode and SEI, and porous electrode behavior for the cathode.

The object of the work is to explore the influence of overcharge and over-discharge conditions on the impedance response of commercial $LiCoO_2$|C batteries. Superposition of impedance spectra, made possible by application of a measurement model analysis, facilitated interpretation of the impedance responses associated with abuse conditions of

Li-ion batteries. Another aim is to explain the kinetics and mass transfer phenomena of Li-ion battery systems with the help of a process model for their impedance response.

CHAPTER 2
LITHIUM-ION BATTERIES

Li-ion batteries are rechargeable (secondary) batteries that are used in a broad range of electronic devices and industry. They have numerous of beneficial properties and characteristics, including high energy density and specific energy, long cycle and shelf life, low self-discharge, no memory effect, and fairly wide operating temperature. Figure 2-1 highlights the relationship between specific and volumetric energy density for the prevalent rechargeable battery technologies. The general goal for battery development is to increase energy and power densities, while minimizing volumetric and mass constraints (i.e. move to the upper right of Figure 2-1). [21] Portable electronics (e.g. cellular phones, laptops, etc.) are an excellent example where consumer demand imposes both smaller and lighter batteries that require minimal time to charge, but without compromising talk time or usable battery life. Such a balance between energy density and rate has propelled lithium ion technology to the forefront. Therefore, in response to these expectations, the next generation of Li-ion batteries will need to achieve higher specific capacities, faster C-rates (time for cell discharge in reciprocal hours), increased safety, and appropriate cyclability. On the other hand they have some shortcomings, such as relatively high material cost, need of a protection circuit to avoid overcharge, over-discharge, and excessive temperature rise and capacity fade [22].

There are three principal components of batteries: electrodes (cathode and anode), electrolyte, and current collectors. The cathode is the positive electrode to which positive ions migrate inside the cell and electrons migrate through the external electrical circuit. The anode is the negative electrode from which electrons are generated to do external work. The electrolyte, which is commonly a liquid solution containing a salt dissolved in a solvent, allows the flow of positive ions, not of electrons, from one electrode to another. The electrolyte must be stable in the presence of both electrodes. The current collectors allow the transport of electrons to and from the electrodes. They are typically metals

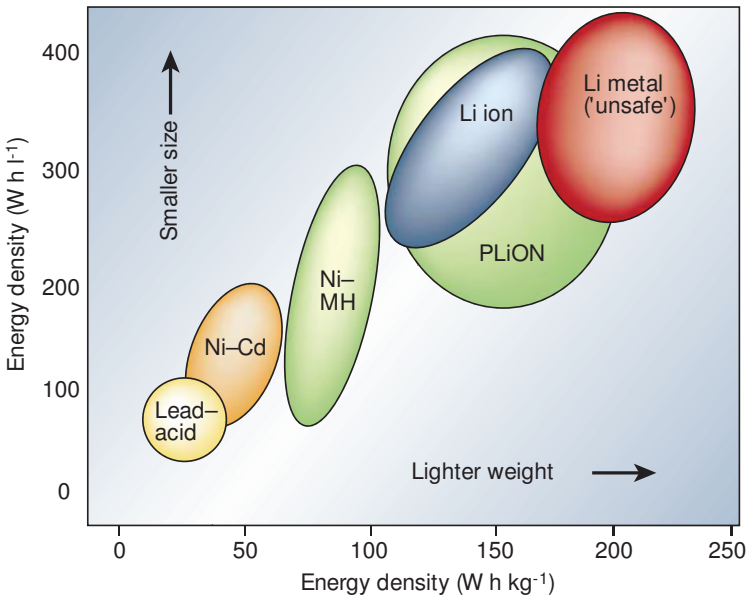

Figure 2-1. Diagram comparing the rechargeable battery technologies as a function of volumetric and specific energy densities. Taken from Tarascon et al. [21].

and must not react with the electrode materials [23]. The Li-ion battery components are illustrated in Figure 2-2. Li-ion batteries generally consist of a lithium metal oxide ($LiMO_2$) as the cathode or positive electrode, lithiated carbon (LiC_6) as the anode or negative electrode, and a lithium salt (i.e. $LiPF_6$ or $LiBF_4$) in a mixture of organic solvents (i.e. ethylene carbonate(EC), propylene carbonate (PC), dimethyl carbonate (DMC), diethyl carbonate (DEC), etc.) as the electrolyte. The current collector for the cathode is usually an aluminum (Al) metal, and the current collector for the anode is copper (Cu).

The active materials in Li-ion batteries operate by reversibly incorporating lithium in an intercalation process, a topotactic reaction where lithium ions are reversibly removed or inserted into a host without a significant structural change to the host. In other words, this process is a transformation, within a crystal lattice, involving the displacement or exchange of atoms. The positive material in a Li-ion cell is a metal oxide with a layered structure. The graphitic carbon negative materials have a layered structure similar to

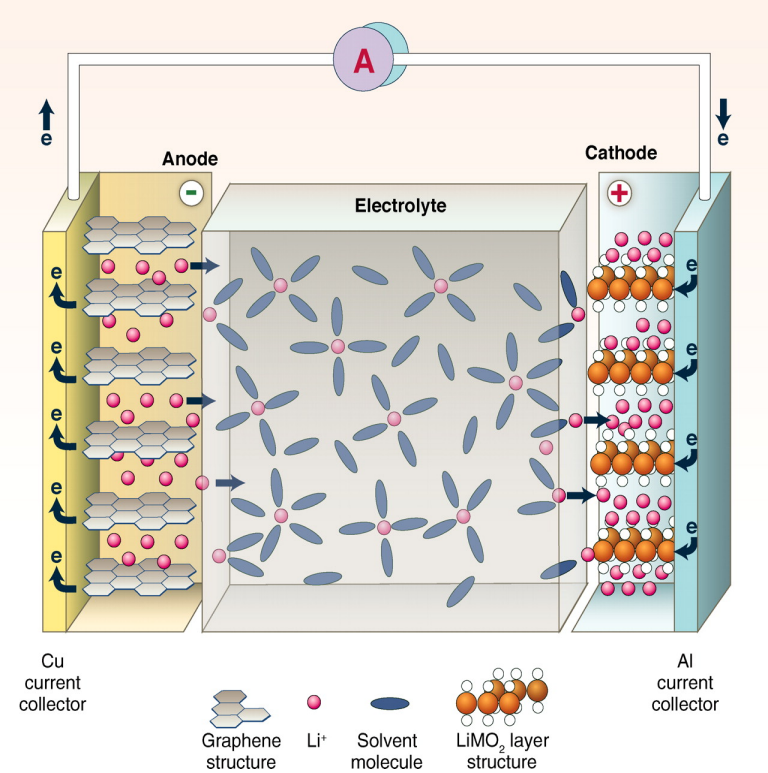

Figure 2-2. Schematic illustrating of general structure and components of a Li-ion battery. The arrows show the direction of discharge. The illustration is taken from Goodenough et al. [23].

graphite. Thus the metal oxide, graphite, and other materials act as hosts, incorporating lithium ions, which act as guests, reversibly to form "sandwich" like structures.

In the charge process of a Li-ion battery, the positive material is oxidized and the negative material is reduced. In this process, lithium ions are de-intercalated from the positive material and intercalated into the negative material, as illustrated in Figure 2-2. In this scheme, $LiMO_2$ represents the metal oxide positive material, such as $LiCoO_2$, and C the carbonaceous negative material, such as graphite. The reverse happens on discharge. As metallic lithium is not present in the cell, Li-ion batteries are chemically less reactive, safer, and offer longer cycle life than possible with rechargeable lithium batteries that employ lithium metal as the negative electrode material. The charge-discharge process in a Li-ion cell is further illustrated graphically in Figure 2-2. In the figure, the layered active materials are shown on metallic current collectors. [24, 25]

When a Li-ion cell is discharged, the anode is electrochemically oxidized, and intercalated lithium ions are released. At the same time, electrons travel through the external circuit to the cathode, as seen in Figure 2-2. When the battery is recharged, the reverse process occurs. As a battery is cycled, lithium ions exchange between the positive and negative electrodes. They are also referred to as rocking-chair batteries as the lithium ions "rock" back and forth between the positive and negative electrodes as the cell is charged and discharged [26].

2.1 Negative Electrode (Anode)

The Li-ion cell negative electrode is composed of a lithium intercalation compound coated in a thin layer onto a metal current collector. The most common anode material is some form of carbon, usually graphite. Carbon is in powder form and combined with binder material. The nature of the carbon can vary considerably: in the source of the graphite (natural or synthetic), purity, particle size, particle size distribution, particle shapes, particle porosity, crystalline phase of carbon, degree of compaction, etc. Anodes composed of silicon, germanium, and titanate ($Li_4Ti_5O_{12}$) materials have also been produced or tested, but at the time of this writing, non-graphitic anodes are rarely implemented. Thin, uniform coatings of active materials are required in lithium-ion batteries that use organic electrolytes almost all commercially available batteries. Thus, the negative electrode material mixing and coating process is often proprietary as variations in processing parameters will affect the resultant coating, and have a strong effect on cell capacity, rate capability, and aging behavior. Anode coating defects can lead to cell failure and cell thermal runaway. [24, 25]

2.2 Positive Electrode (Cathode)

There are several types of positive electrode materials used in Li-ion batteries. These materials are powders that are combined with binder and conductivity enhancers (carbon), and deposited onto a current collector in a thin layer form. The most common cathode material in Li-ion batteries is lithium cobalt oxide ($LiCoO_2$). However, various

other materials are used such as lithium iron phosphate ($LiFePO_4$), spinels such as lithium manganese oxide ($LiMn_2O_4$), or mixed metal oxides that include cobalt (Co), nickel (Ni), aluminum (Al), and manganese oxides such as nickel cobalt aluminate (NCA) material ($LiNi_{0.8}Co_{0.15}Al_{0.05}O_2$) and nickel manganese cobaltite (NMC) material ($LiNi_{1/3}Mn_{1/3}Co_{1/3}O_2$). As with negative electrode materials, positive electrode materials can also vary considerably based on source, particle characteristics, purity, coatings on particles, crystallinity, mixture ratios of various components, degree of compaction, etc. Based on thermal stability measurements of the cathode materials with electrolyte at full-charge potential conditions, it is shown that cathode materials begin to react exothermically with electrolyte at a range of temperatures from approximately 130 - 250°C (270 - 480°F). [24, 25]

2.3 Electrolyte

The electrolyte in a Li-ion cell is typically a mixture of organic carbonates such as ethylene carbonate or diethyl carbonate. The mixture ratios vary depending upon desired cell properties, e.g., a cell designed for low-temperature applications will likely contain a lower viscosity electrolyte than one optimized for room temperature applications. These solvents contain solvated lithium ions, which are provided by lithium salts, most commonly lithium hexafluorophosphate ($LiPF_6$). Cell manufacturers typically include low concentrations of a variety of additives to improve performance characteristics such as cycle life, calendar life, overcharge impedance, and cell stability.

At typical cell potentials, mixtures of lithiated carbon (or lithium metal) and organic electrolyte are not thermodynamically stable, and a reaction between the two materials will occur. At room temperature conditions, the result of this reaction is the formation of a passivating layer on the carbon surface, commonly referred to as the solid-electrolyte interphase (SEI) and some gases that result from breakdown of the electrolyte (short chain hydrocarbons, carbon dioxide, etc.). During cell manufacturing, after cell assembly, the cell is slowly charged and discharged (and possibly repeatedly cycled) during what

is called "cell formation". This formation process is designed to produce a stable and uniform SEI layer on the cell anode to protect and support it.

As temperature increases, reaction rates between the electrolyte and lithiated carbon increase exponentially, i.e., following Arrhenius behavior. Therefore, Li-ion cell capacity fades and internal impedance growth accelerates with increased ambient temperatures. Most Li-ion batteries are not designed to be stored or operated above approximately 60°C (140°F). Many soft-pouch cell, or even coin-cell designs exhibit swelling if operated or stored at 60°C or above, due to gas generation from reactions similar to those responsible for SEI-formation. For most commercial Li-ion chemistries, the SEI layer itself will collapse when cell temperature reaches the range of 75 - 90°C (167 - 194°F) where the exact temperature depends upon cell chemistry and SOC.

The most commonly used electrolyte salt ($LiPF_6$) will decompose to form hydrofluoric acid (HF) if mixed with water or exposed to moisture. Cell manufacturing and assembly is conducted in "dry rooms" to prevent HF formation since the presence of HF in cells will cause degradation of the cells. Leakage of free electrolyte from cells can result in deposition of the electrolyte salt as organic components evaporate.[24, 25]

CHAPTER 3
ELECTROCHEMICAL IMPEDANCE SPECTROSCOPY

One of the most important and fundamental laws of physics is that of Ohm's law. This law defines the relationships between potential (voltage), current and resistance in an ideal conductor. Ohm's law states that the current (I) through a conductor between two points is directly proportional to the potential difference (V) across the two points. This constant ratio is the resistance (R) of the conductor. This is described mathematically by

$$R = \frac{V}{I} \tag{3–1}$$

The applied current is direct (dc) for this type of ideal electrochemical system. However, as shown in Figure 3-1, if the applied potential is oscillated by a sinusoidal wave, the current will be converted to alternative (ac). The proportionality will turn out to be a complex number due to the sinusoidal perturbation. This term is called impedance and shown by equation 3–4.

$$Z = \frac{\widetilde{\Delta V}}{\widetilde{\Delta I}} = \frac{|\Delta V|}{|\Delta I|} e^{\mathrm{j}\theta} = Z_{\mathrm{r}} + \mathrm{j}Z_{\mathrm{j}} \tag{3–2}$$

where $\widetilde{\Delta V}$ is the input, and $\widetilde{\Delta I}$ is the output signal. $\widetilde{\Delta V}$ is the change in the oscillated potential, whereas $\widetilde{\Delta I}$ is the change in the current response with respect to the perturbed potential. Therefore, impedance is a transfer function which is the ratio of an input oscillating potential and an output ac current, or vice versa. When the perturbation, which is either potentiostatic or galvonastatic (current perturbation), is applied with a range of frequency, one can get a spectrum of impedance results. In other words, an impedance spectra is obtained by having the responses of oscillation at each frequency.

Impedance spectroscopy is an experimental method for analyzing and characterizing electrochemical systems. Electrochemical systems with a single faradaic reaction with a semi-infinite linear diffusion can be represented by a simple Randles circuit, which is illustrated in Figure 3-2, where R_e is electrolyte or ohmic resistance, R_t is charge-transfer resistance, C_{dl} is double-layer capacitance, and Z_W is the Warburg impedance. The

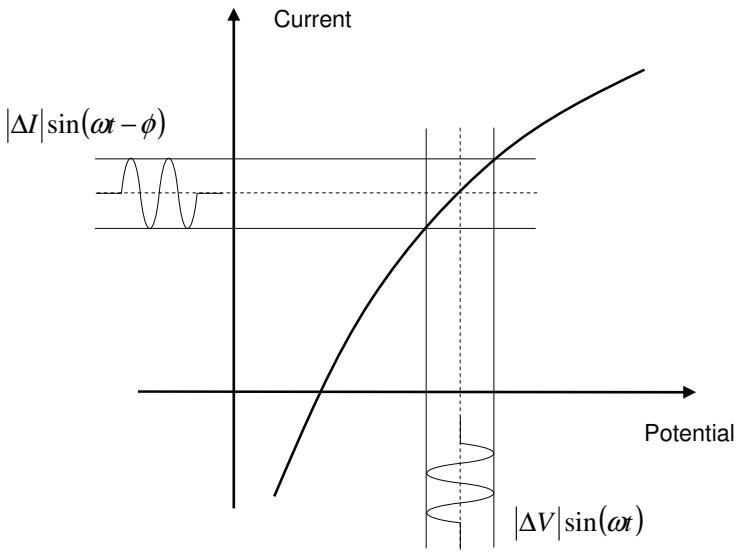

Figure 3-1. Polarization curve and representation of impedance.

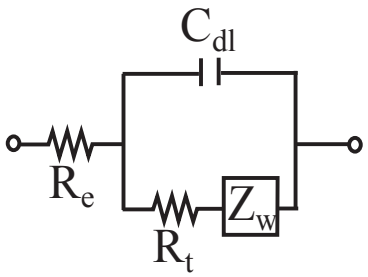

Figure 3-2. A schematic representation of a Randles circuit.

impedance associated with this system can be expressed as

$$Z(\omega) = \mathrm{R_e} + \frac{\mathrm{R_t} + \mathrm{Z_W}}{1 + \mathrm{j}\omega(\mathrm{R_t} + \mathrm{Z_W})\mathrm{C_{dl}}} \tag{3–3}$$

The Warburg impedance is an element corresponding to the semi-infinite linear diffusion in an electrochemical system and its equation is

$$Z_{\mathrm{W}}(f) = \frac{A_{\mathrm{W}}}{\sqrt{2\pi \mathrm{j} f}} \tag{3–4}$$

where A_{W} is the Warburg coefficient and f is frequency.[27] An impedance representation of this system is shown in Figure 3-3, which has a perfect semi-circle at high and middle

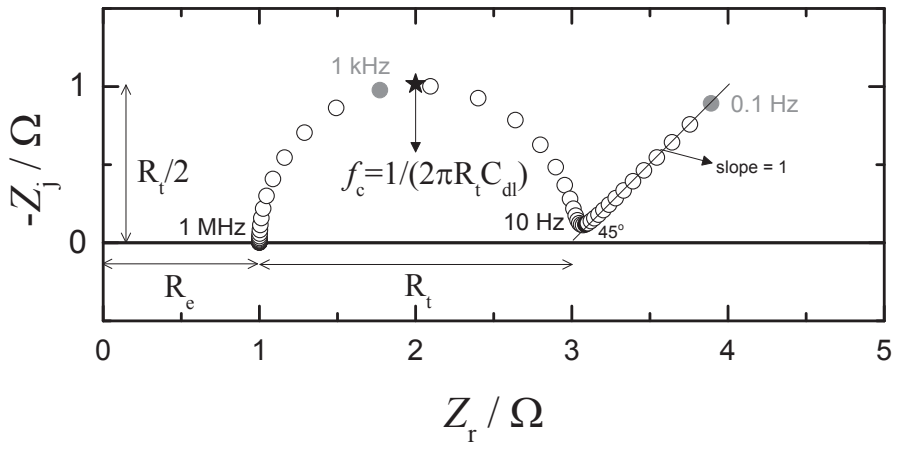

Figure 3-3. The simulation of an impedance spectrum of equation 3–3 in Nyquist format for the Randles circuit. Here, the values of the circuit elements are R_e= 1 Ω, R_t= 2 Ω, C_{dl}= 100 μF, A_W= 1 Ω $s^{-0.5}$, and f_c= 795.77 Hz.

frequencies and a line with 45° angle or slope of 1 at low frequency. Other electrochemical parameters and their values are depicted in Figure 3-3. Here, there is one time constant. However, the impedance response of electrochemical systems rarely shows the ideal response expected for single electrochemical reactions. The impedance response typically reflects a distribution of time constants that is commonly represented in equivalent electrical circuits as a constant phase element (CPE). Time-constant dispersion can be observed due to variation along the electrode surface of reactivity or of potential and current. [27]

The impedance associated with a simple electrochemical reaction with a diffusion can be expressed in terms of a CPE as

$$Z(\omega) = \mathrm{R_e} + \frac{\mathrm{R_t} + \mathrm{Z_d}}{1 + (\mathrm{j}\omega)^{\alpha}(\mathrm{R_t} + \mathrm{Z_d})\mathrm{Q}} \tag{3–5}$$

where Z_d is the diffusion impedance. In this case, a suppressed semi-circle would be seen instead of a perfect one in the Nyquist plot in Figure 3-3.

CHAPTER 4
EXPERIMENTAL METHOD

Electrochemical experiments were performed on commercial $LiCoO_2$|C coin cells. Impedance spectroscopy was used to monitor changes associated with different states-of-charge, imposition of overcharge, and imposition of over-discharge.

4.1 Materials

Commercial secondary LIR2032 button (or coin) cells were purchased from AA Portable Power Corp. (Richmond, CA, www.batteryspace.com) and BatteryJunction.com (Old Saybrook, CT, www.batteryjunction.com). LIR refers to Lithium-ion rechargeable, and the 2032 specification means that the batteries were 20 mm in diameter and 3.2 mm in height. The cathode was $LiCoO_2$, the separator was Celgard 8 μm, and the anode was carbon. The coin battery is illustrated in Figure 4-1. The back (positive side) and front (negative side) sides of the battery are shown in Figure 4-1A. When the battery is unsealed, three small sheets folded on top of each other will be seen: a polymer sheet between two metal sheets, which are shown in in Figure 4-1B. The polymer sheet is the separator: whereas, the metal sheets are the carbon anode deposited on a copper (Cu) current collector and the $LiCoO_2$ cathode deposited on a aluminum (Al) current collector.

The normal operating potential range of the cells reported by the supplier [28], between 3.00 V (0% state-of-charge) and 4.20 V (100% state-of-charge), is in agreement with published literature [29–31].

4.2 Instrumentation

Electrochemical experiments and impedance measurements were performed using a Gamry PCI4/750 Potentiostat connected to a desktop computer. Gamry's Virtual Front Panel (VFP600) and Electrochemical Impedance Spectroscopy (EIS300) software packages were used to run the experiments. The primary purpose of the potentiostat in these experiments was to maintain a constant cell potential while measuring the impedance.A

A B

Figure 4-1. The photograph of the LIR2032 coin cell; A) positive and negative contacts and B) anode, separator, and cathode removed from the coin cell.

Tenney Jr. environmental test chamber was used to control the temperature of a battery and its surroundings.

4.3 Protocol

Following the previous work [32], the impedance response was analyzed throughout the normal potential range under charge and discharge profiles. The impedance was also analyzed under overcharge and over-discharge conditions. Capacity measurements were used to show the extent to which the overcharging and over-discharging processes affected battery performance. These experiments were performed at room temperature (around 20 °C) with the batteries which were purchased from AA Portable Power Corporation.

As received, the $LiCoO_2$|C cells had an open-circuit potential of 3.8±0.2 V. The cells were slowly charged under galvanostatic control at a current of 2 mA to 4.20 V. To assess the capacity of the battery, each cell was subsequently discharged to 3 V at a constant 30 mA current (the nominal 1C rate) and charged back to 4.20 V with the same constant 30 mA current. During charge or discharge throughout the normal range, the capacity was obtained by multiplying the amount of applied current with the time elapsed. The

average measured value for the capacity of the LIR2032 battery at 1C rate was 30 mAh, in agreement with the vendor documentation [28, 33].

For impedance measurements in the normal potential range, the cells were held for at least one hour at a constant cell potential of 4.20 V. After the constant-potential rest period, the impedance was measured using a 10 mV perturbation and 100 kHz - 20 mHz frequency range. As suggested by Hirschorn et al. [34], the linear response of low-frequency Lissajous plots was used to ensure linearity during the impedance measurement. Three replicated impedance scans were obtained for each condition tested. Following impedance measurements at a given potential, the cell potential was modified for the discharge profile in 0.20 V increments down to and including 3.00 V. The change in potential was conducted galvanostatically at a 2 mA current. For each potential step, the battery was allowed to stabilize for a period of one hour, in which the current was reduced to a value that was smaller than 0.02 mA. Impedance measurements were made in triplicate following stabilization at the desired potential. The charge profile, following the same procedure, was executed immediately up to and including 4.20 V.

The effect of overcharging and over-discharging a $LiCoO_2$|C cell was also analyzed. To assess the influence of overcharging the battery, the cell was initially charged under constant 2 mA current to 4.20 V. Impedance measurements were performed at each 0.08 V step up to and including 5.00 V. As before, a 10 mV ac perturbation and 100 kHz-20 mHz frequency range were implemented. A similar protocol was followed for the over-discharge. Another cell was initially discharged under constant current to 3.00 V. Impedance measurements were performed at each 0.08 V step down to and including 2.20 V. Capacity measurements, using constant 30 mA current for both charging and discharging, were obtained before and after the overcharge and over-discharge protocols to quantify changes in battery performance.

Another set of $LiCoO_2$|C batteries, purchased from BatteryJunction.com, were analyzed with using impedance spectroscopy and capacity measurements at different

surrounding temperature. The temperature was applied between -20 and 60 °C with 10 °C increments with using the environmental temperature chamber. The batteries is held for 30 minutes at each temperature to reach a uniform and stable condition. Impedance measurements were performed at 4 V under same amount of ac perturbation, 10 mV, and frequency range, 100 kHz - 20 mHz. The same procedure was applied for the capacity measurements, at 1C discharge rate.

All of the experiments were repeated 3-4 times with same type of battery to ensure that the results were both consistent and reproducible. The software incorporated in the Gamry system enabled consistent and precise procedures to be performed which served to reduce errors among the repetitive experiments.

CHAPTER 5
RESULTS AND DISCUSSION

The impedance response of the $LiCoO_2$|C coin cells is presented for state-of-charge, overcharge, and over-discharge conditions.

5.1 State-of-Charge

The impedance response for a commercial $LiCoO_2$|C coin cells is presented in Figure 5-1 with cell potential from 3 to 4.2 V as a parameter. These results represent the impedance response under normal operating conditions and under the discharge profile. Results obtained under the charge profile were identical. Notably, the impedance was significantly larger at 3 V, especially at the low frequencies, even though it became smaller while the potential approached to the upper limit in the normal operating range for the $LiCoO_2$|C coin cell. While many factors contribute to selection of the operational potential range of a battery, the impedance results suggest that 3.2 V would be a more appropriate lower limit for the normal potential range.

5.2 Overcharge

The impedance is a strong function of cell potential. To explore the sensitivity of impedance spectroscopy for overcharging the battery, the coin cell potential was increased in 80 mV increments starting from 4.2 V and the impedance was measured after the cell current approached zero, i.e., 0.02 mA. To make the features visible, the impedance response is presented in a sequence of plots. The impedance response is presented in Figure 5-2 for cell potential ranging from 4.20 to 4.44 V (Figure 5-2A) and potential ranging from 4.44 to 4.60 V (Figure 5-2B). The impedance at potentials up to 4.52 V were almost identical. Superposition of impedance diagrams suggests that the reactions taking place are not affected by potential in this range and that an upper value for the normal operating range could be 4.5 V. The impedance at 4.6 V is strikingly different, in agreement with the results reported by Belov and Yang [7] and Love and Swider-Lyons [8].

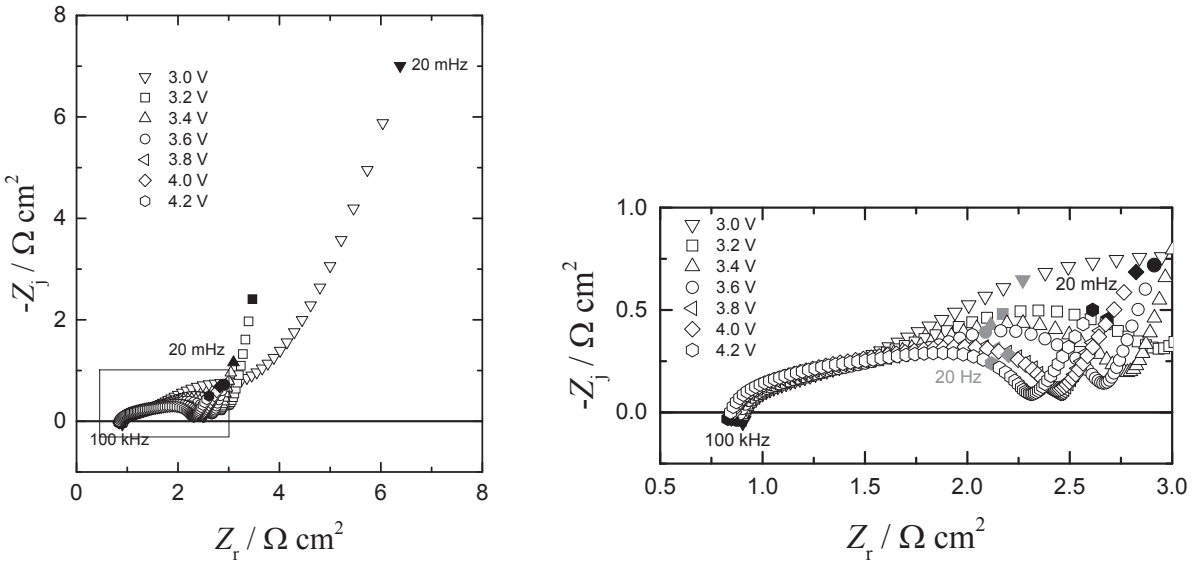

Figure 5-1. Impedance response in Nyquist format for a $LiCoO_2$|C coin cell under normal operating conditions with cell potential as a parameter: A) complete spectra and B) low impedance values corresponding to the box in (A). The impedance was measured under the discharge profile. Results obtained under the charge profile were identical. Taken from Erol et al. [35]

The impedance values grew dramatically from a potential of 4.6 V to 4.76 V, as shown in Figure 5-3. In Figure 5-3A, a substantial growth in the low-frequency impedance is seen for the transition from 4.6 V to 4.76 V. The zoomed image in Figure 5-3B indicates comparatively smaller amount of differences in the high-frequency response.

The impedance response is presented in Figure 5-4 for potentials ranging from 4.76 to 5.00 V. In contrast to the results presented in Figure 5-3, a capacitive loop is evident at low frequencies for cell potentials above 4.92 V. In addition, as seen in the zoomed image in Figure 5-4B, the size of the capacitive loop at high frequencies increases with potential for potentials greater than 4.76 V.

After overcharging to a potential of 5 V, the battery was allowed to relax for two days at the open-circuit condition. When held at open-circuit, the potential of the overcharged battery rapidly decreased for the first two hours and then slowly approached the normal operating range for the rest of the time, as shown in Figure 5-5.

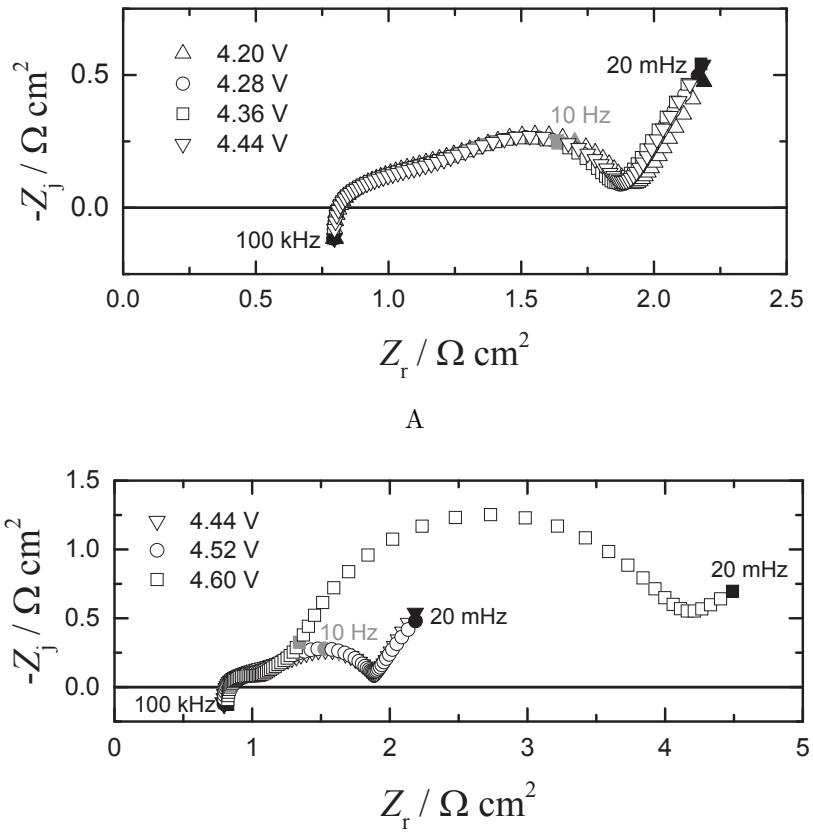

Figure 5-2. Impedance response in Nyquist format for a $LiCoO_2$|C coin cell under overcharge conditions with cell potential as a parameter: A) potential ranging from 4.20 to 4.44 V; and B) potential ranging from 4.44 to 4.60 V. Taken from Erol et al. [35]

During self-discharge after overcharging to 5 V, impedance measurements were collected as a function of time to show the evolution of the impedance response during the self-discharge. The results given in Figure 5-6 show that the impedance increased as the cell potential approached values within the normal operating range. The major change was seen in the low-frequency part of the spectrum as revealed in Figure 5-6A. The zoomed image shown in Figure 5-6B reveals that the high-frequency capacitive loop did not change very much.

After the self-discharge period, the overcharged battery was discharged to 4 V, a potential within the normal range. A dramatic difference on the impedance between

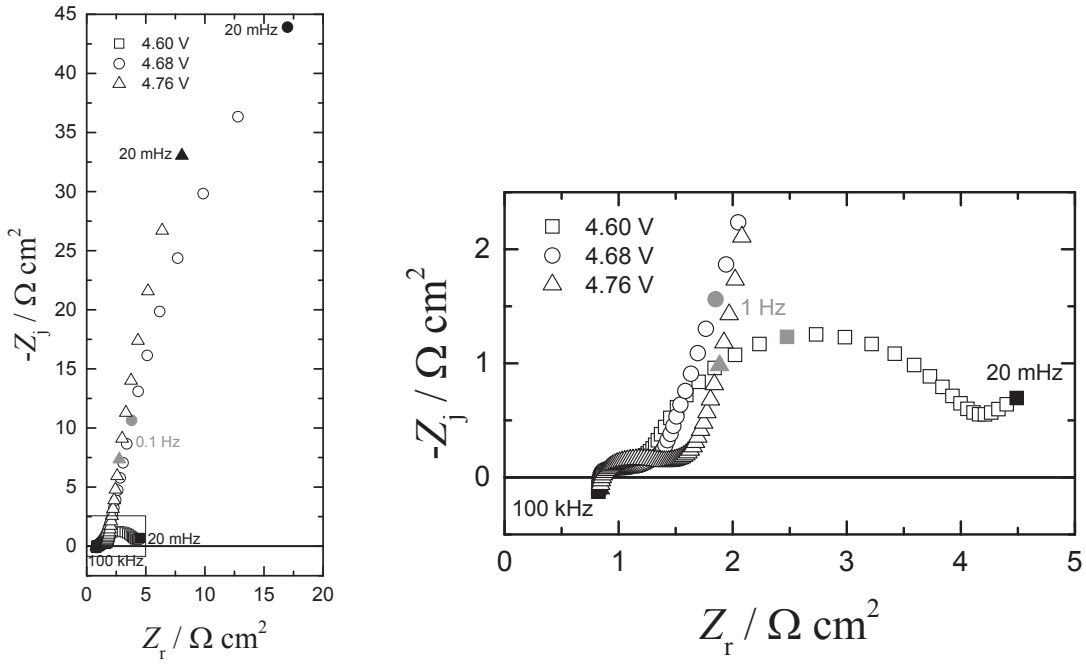

Figure 5-3. Impedance response in Nyquist format for a $LiCoO_2$|C coin cell under overcharge conditions with cell potential, ranging from 4.60 to 4.76 V, as a parameter: A) complete spectra and b) smaller impedance values corresponding to the box in (B). Taken from Erol et al. [35]

a pristine cell and an overcharged cell is seen in Figure 5-7. Both high-frequency capacitive loops and the low-frequency parts of the impedance responses are distinctly altered. The capacity results for before and after overcharging the cell are presented in Figure 5-8. For both the pristine and overcharged cells, the capacity measurements were made at a relatively large 1C rate after only one charge-discharge cycle. Thus, the capacity on discharge at a fixed 30 mA rate was larger than it was during the subsequent charge. According to Buiel and Dahn [36], this difference may be attributed to the consumption of lithium ions by reactions that increase the SEI layer thickness. The capacity difference between the pristine and overcharged batteries at both the fully-charged and fully-discharged condition was roughly 4.5 mAh, which corresponds to a 15% capacity loss at the end of the discharge step and a 20% capacity loss at the conclusion of the charge step.

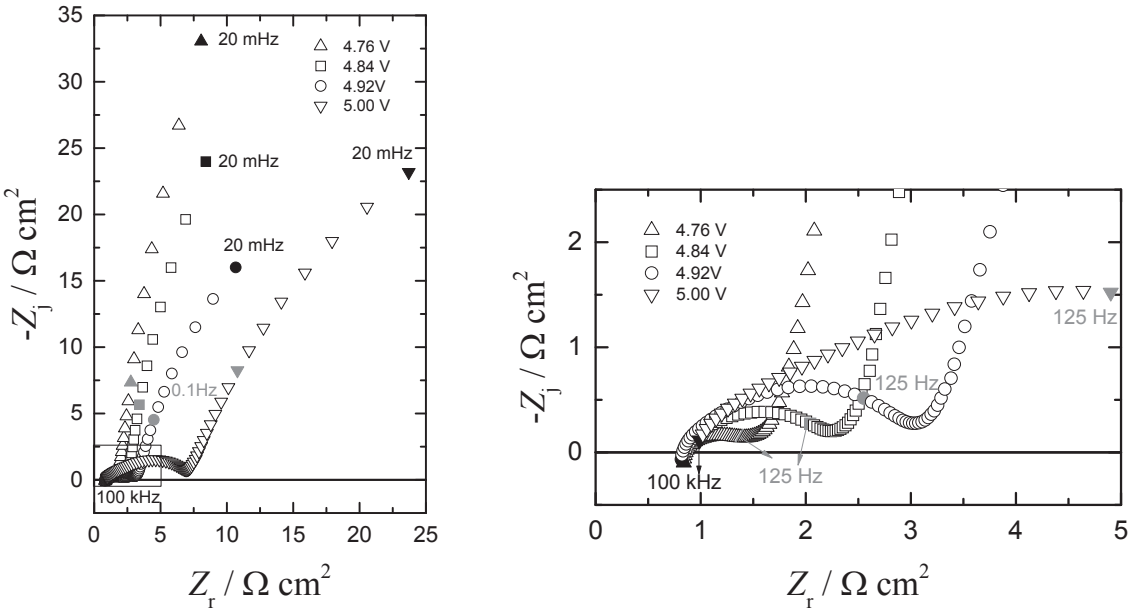

A B

Figure 5-4. Impedance response in Nyquist format for a $LiCoO_2$|C coin cell under overcharge conditions with cell potential, ranging from 4.76 to 5.00 V, as a parameter: A) complete spectra and B) high frequency values corresponding to the box in (A). Taken from Erol et al. [35]

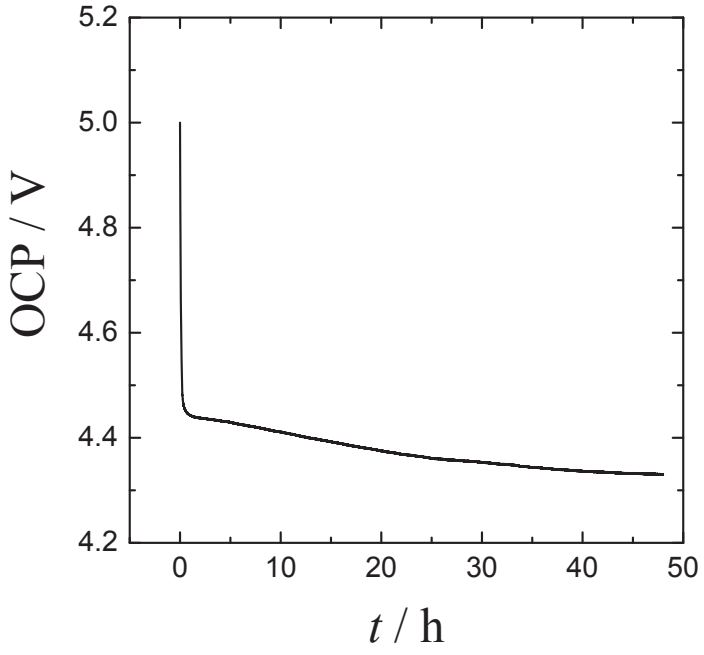

Figure 5-5. Open-circuit potential as a function of time for an overcharged $LiCoO_2$|C coin cell. Taken from Erol et al. [35].

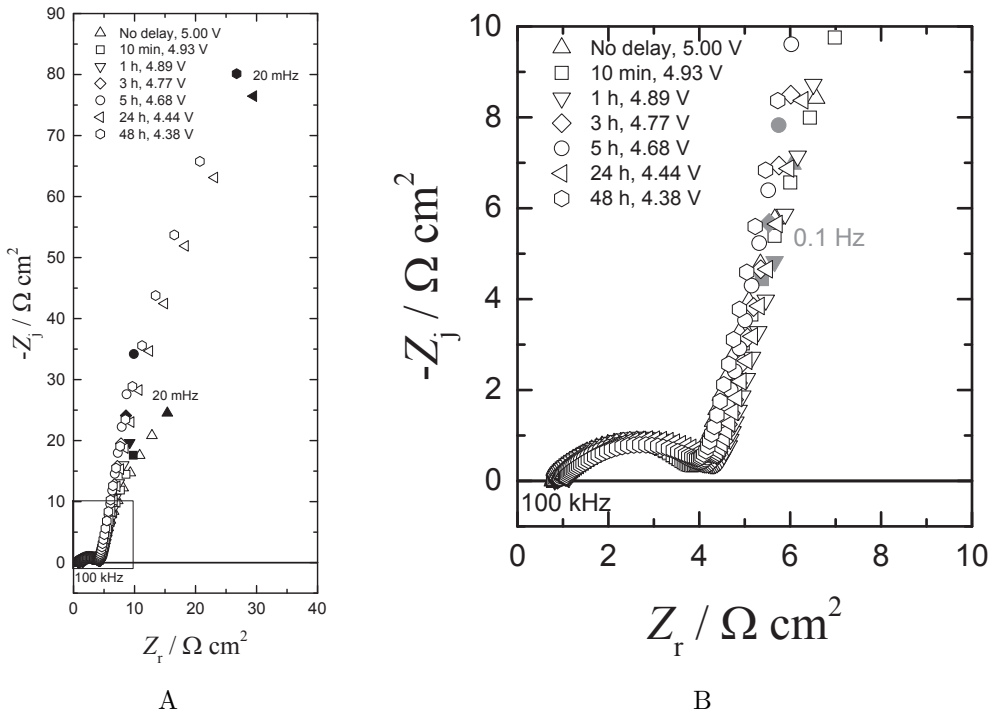

Figure 5-6. Impedance response in Nyquist format for a $LiCoO_2$|C coin cell during self-discharge under overcharge conditions with elapsed time as a parameter; A) complete spectra and B) high frequency values corresponding to the box in (A). Taken from Erol et al. [35]

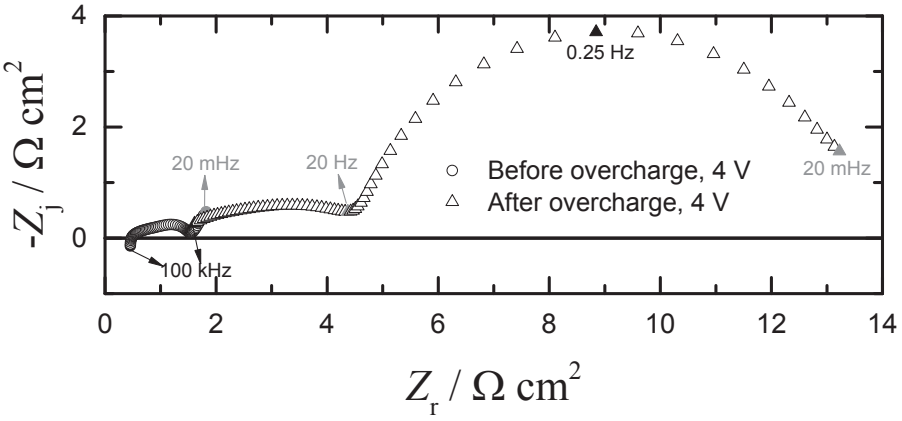

Figure 5-7. Impedance response of a $LiCoO_2$|C coin cell at a potential of 4 V before and after the cell was overcharged. Taken from Erol et al. [35]

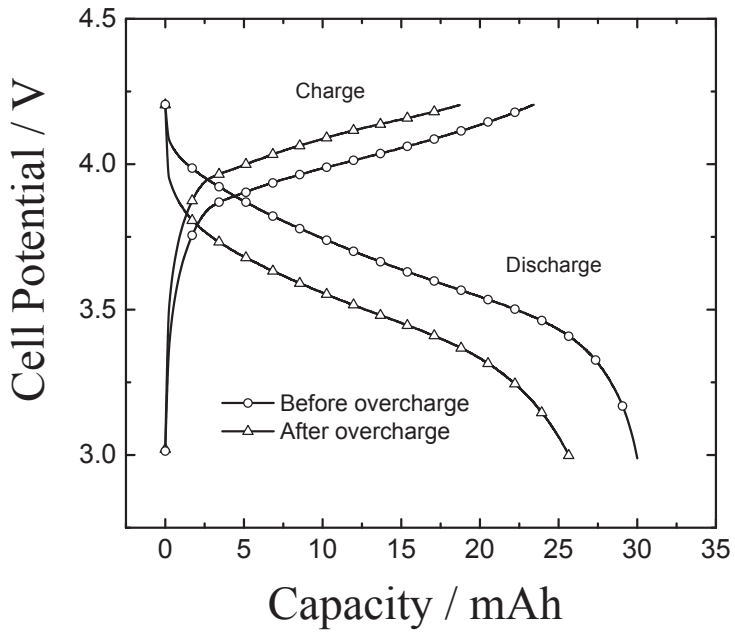

Figure 5-8. Discharge and charge capacity of a $LiCoO_2$|C coin cell before and after the cell was overcharged. Charge and discharge were at a constant 30 mA current (nominally a 1C rate of discharge). Symbols used to distinguish lines are placed at an interval of 20 measurements. Taken from Erol et al. [35].

5.3 Over-Discharge

The cell potential was decreased in 80 mV increments starting from 3 V, and the impedance was measured after the cell current approached zero to explore the sensitivity of impedance spectroscopy to over-discharging the battery. The impedance was again a strong function of cell potential as observed in the overcharging case. The impedance response is presented in Figure 5-9 for cell potential ranging from 3.00 to 2.84 V. The zoomed image in Figure 5-9B reveals that the high-frequency loop disappeared as the battery was subjected to over-discharge. The impedance response is presented in Figure 5-10 for cell potential ranging from 2.84 to 2.60 V (Figure 5-10A), potential ranging from 2.60 to 2.36 V (Figure 5-10B), and potential ranging from 2.36 to 2.20 V (Figure 5-10C). High-frequency results are not shown in these figures since most of the change in the impedance at different potentials came from the low-frequency part. The low-frequency

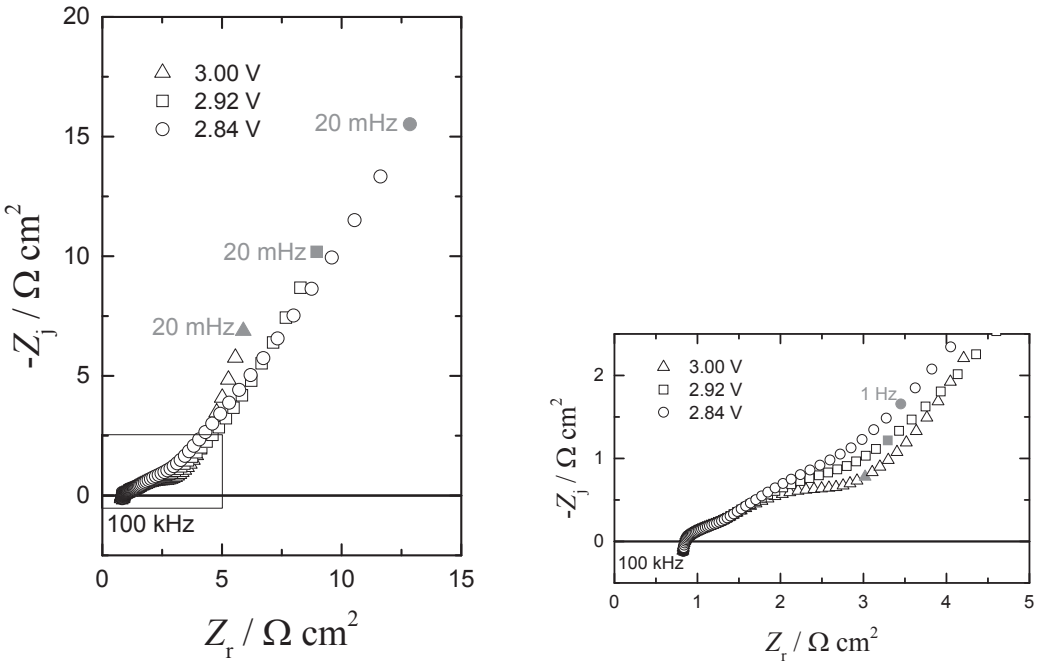

Figure 5-9. Impedance response in Nyquist format for a $LiCoO_2$|C coin cell under over-discharge conditions with cell potential, ranging from 3.00 to 2.84 V, as a parameter: A) complete spectra and B) high frequency values corresponding to the box in (A). Taken from Erol et al. [35]

part of the impedance response became larger as the cell potential decreased under over-discharge conditions.

After over-discharging to a potential of 2.20 V, the battery was allowed to relax for two days at the open-circuit condition. When held at open-circuit, the over-discharged battery slowly reached a cell potential within the normal operating range, as shown in Figure 5-11.

During self-charge after over-discharging to 2.2 V, impedance measurements were collected as a function of time to show the evolution of the impedance response during the self-charge. The results are shown in Figure 5-12. The impedance increased over the first 3 hours and then began to decrease for the measurement taken at 5 hours. After 48 hours, the impedance was similar to that obtained before the potential excursion.

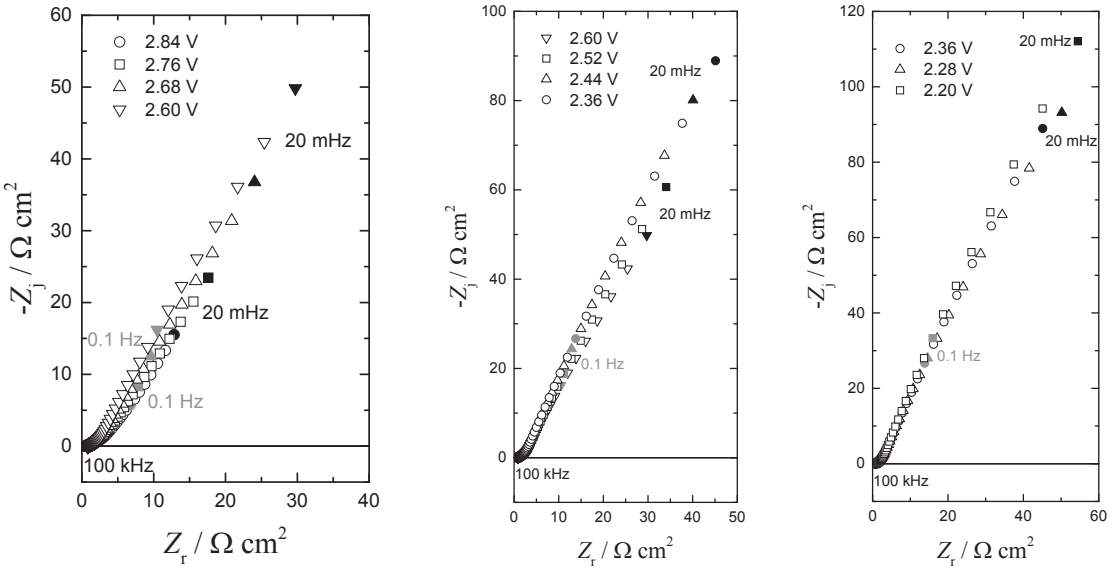

Figure 5-10. Impedance response in Nyquist format for a $LiCoO_2$|C coin cell under over-discharge conditions with cell potential as a parameter: A) potential ranging from 2.84 to 2.60 V; B) potential ranging from 2.60 to 2.36 V, and C) potential ranging from 2.36 to 2.20 V. Taken from Erol et al. [35]

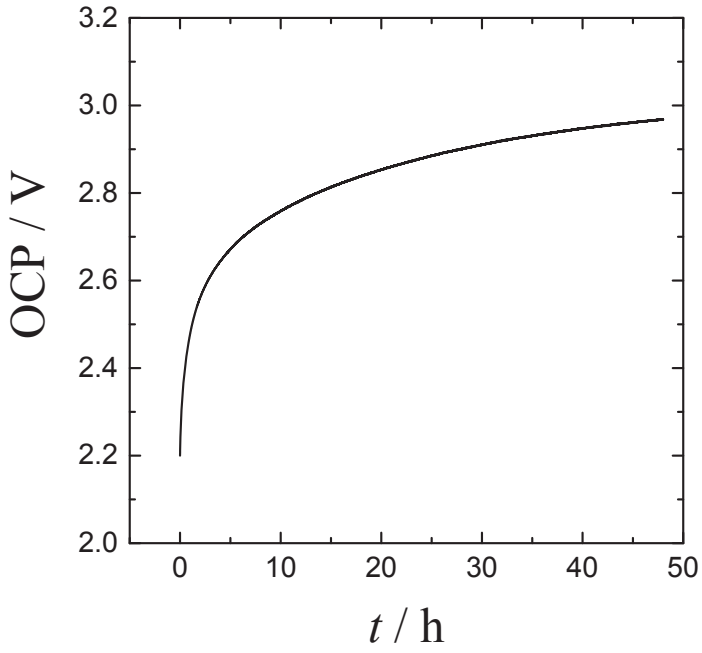

Figure 5-11. Open-circuit potential as a function of time for an over-discharged $LiCoO_2$|C coin cell. Taken from Erol et al. [35]

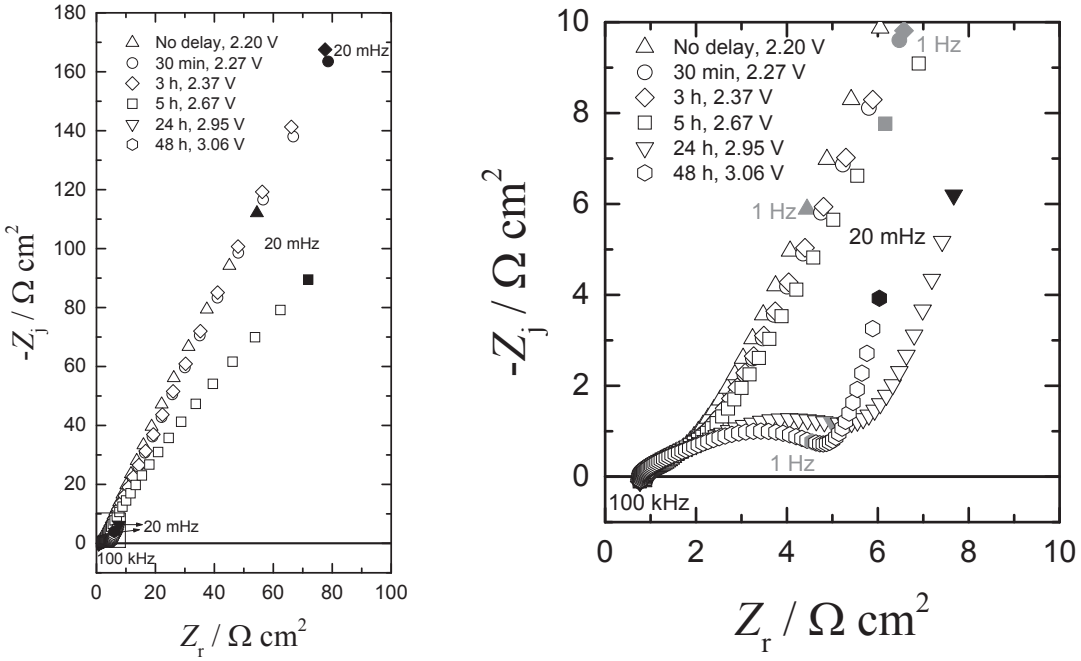

Figure 5-12. Impedance response in Nyquist format for a $LiCoO_2$|C coin cell during self-charge under over-discharge conditions with elapsed time as a parameter; A) complete spectra and B) high frequency values corresponding to the box in (A). Taken from Erol et al. [35]

The impedance response and capacity measured before and after the cell was over-discharged are presented in Figure 5-13 and 5-14, respectively. The results are in striking contrast to the results seen for the overcharged battery (Figures 5-7 and 5-8). Minor differences at the capacity (presumably due to the cycling) and the impedance (due to only ohmic resistance) are observed in these results. It should be noted, however, that Maleki and Howard [5] over-discharged the Li-ion batteries to lower potentials and observed a capacity fade for the batteries.

The changes of the composition and the surface topography of both cathode and anode, respectively, after overcharge and over-discharge processes are shown in Figures 5-15 and 5-16. It can be seen that the cathode particles are distributed on the metal surface (Al) nonuniformly in Figures 5-15B, 5-15D, and 5-15F. There are fewer pores at the cathode for the over-discharged cell as seen in Figure 5-15E compared to Figures

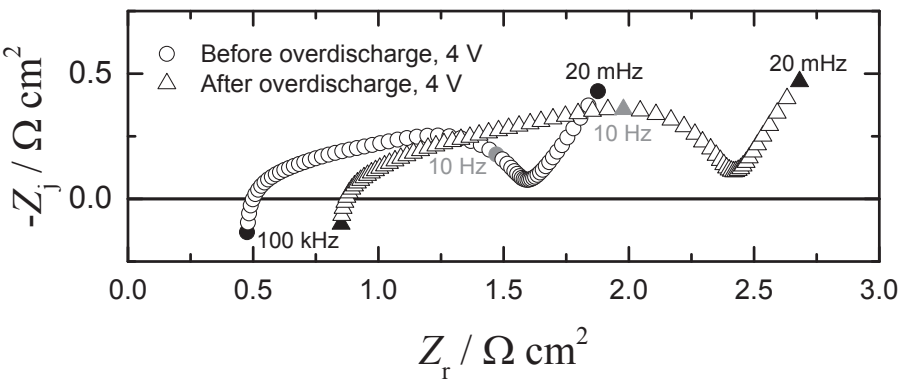

Figure 5-13. Impedance response of a $LiCoO_2$|C coin cell at a potential of 4 V before and after the cell was over-discharged. Taken from Erol et al. [35].

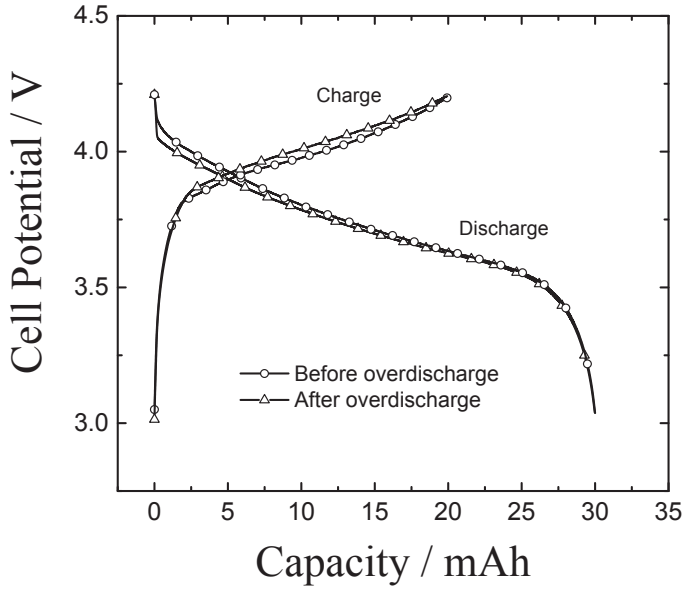

Figure 5-14. Discharge and charge capacity of a $LiCoO_2$|C coin cell before and after the cell was over-discharged. Charge and discharge were at a constant 30 mA current (nominally a 1C rate of discharge). Symbols used to distinguish lines are placed at an interval of 20 measurements. Taken from Erol et al. [35]

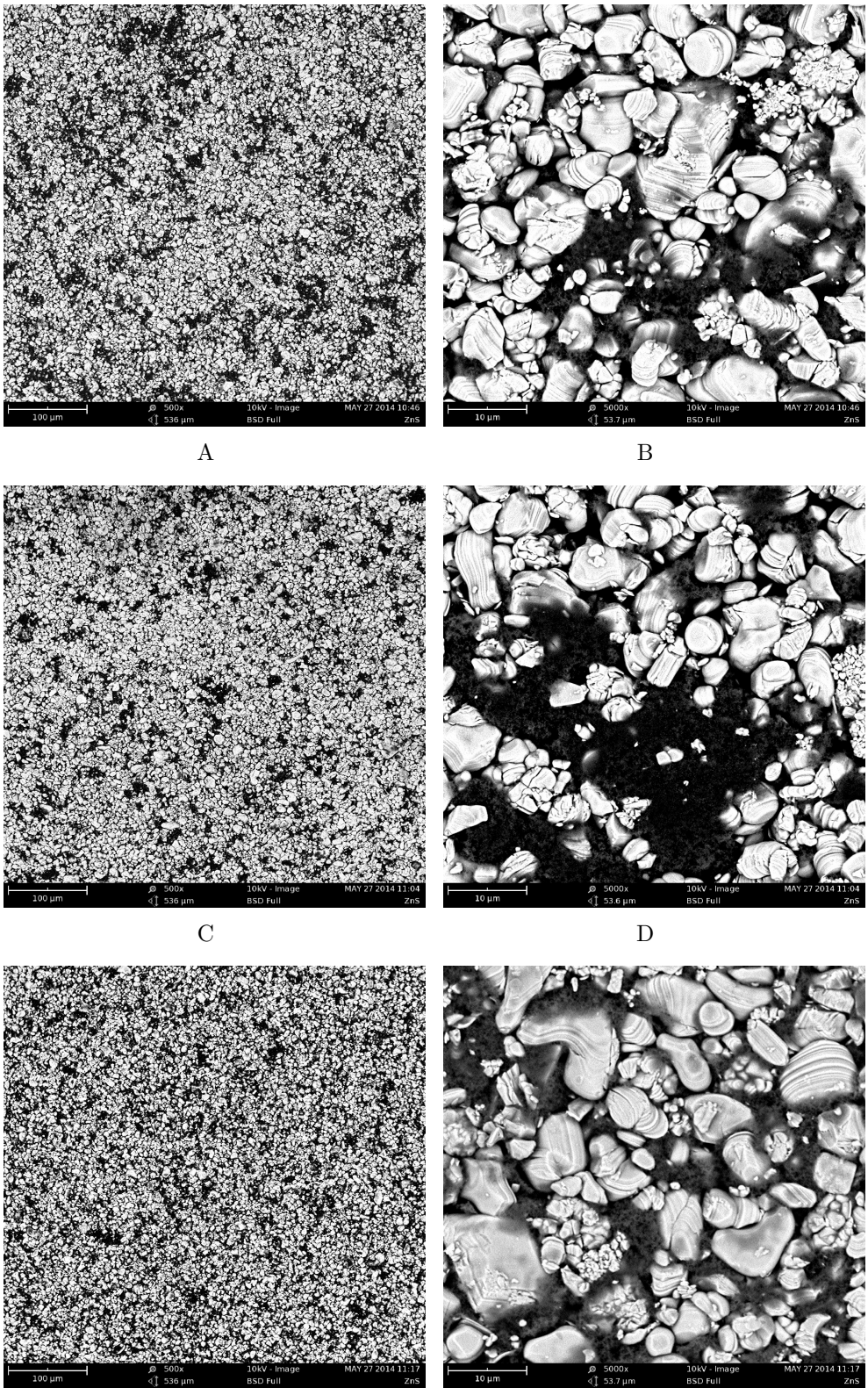

Figure 5-15. SEM micrographs of the $LiCoO_2$ cathode: A) a pristine cell; B) higher magnification of (A); C) an overcharged cell; D) higher magnification (C); E) an over-discharged cell; F) higher magnification of (E)

5-15A and 5-15C. The reason for that is greater amount of lithium ions are packed in the cathode while over-discharging. As seen in Figures 5-16A, 5-16C, and 5-16E, the anode particles are more like in plate-shaped, and the particle size is more uniform than of the cathode. The anode particles are covered with a different layer when the battery is overcharged or over-discharged which can be seen in Figures 5-16D and 5-16F compared to Figure 5-16B. This layer will be explained in Section 6.2.1.1.

5.4 Temperature

The temperature of a $LiCoO_2$|C coin cell was elevated with 10 °C increments starting from 20 °C up to and including 60 °C with using the temperature control chamber. The impedance result at each step presented in Figure 5-17 shows that the high-frequency capacitive loop gets smaller as increasing the temperature. However, the capacitive loop at 60 °C altered distinctly. The ambient temperature at this level may cause damage to the battery, i.e., the electrolyte might evaporate. The slopes of low frequency lines, on the other hand, gets closer to 45° as the temperature rises. The capacity change is shown in Figure 5-18 where there is a slight growth in capacity as the temperature increases.

The impedance and the capacity measurements were achieved at low temperature after high temperature measurements. A similar protocol was followed for the low temperature measurements. The temperature of a coin cell was decreased with 10 °C increments starting from 20 °C down to and including -20 °C. The impedance result at each step presented in Figure 5-19 shows that the impedance grows dramatically as decreasing the temperature. The high-frequency capacity loops get larger and the low-frequency tail disappears under freezing point, 0 °C. The capacity change is shown in Figure 5-20 which can be seen that there is a big capacity loss due to the increase in the impedance as the temperature decreases.

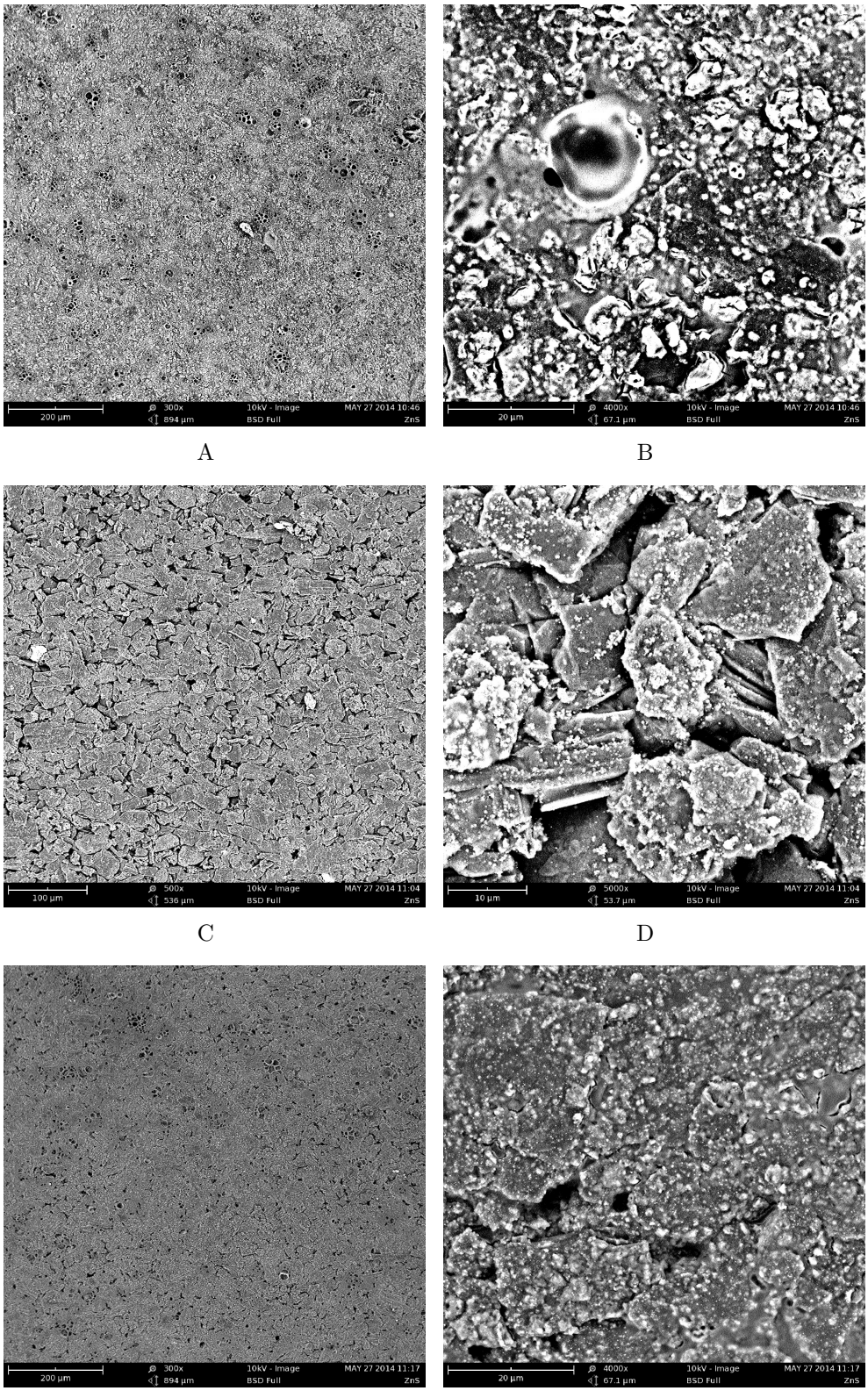

Figure 5-16. SEM micrographs of the carbon anode: A) a pristine cell; B) higher magnification of (A); C) an overcharged cell; D) higher magnification of (C); E) an over-discharged cell; F) higher magnification of (E)

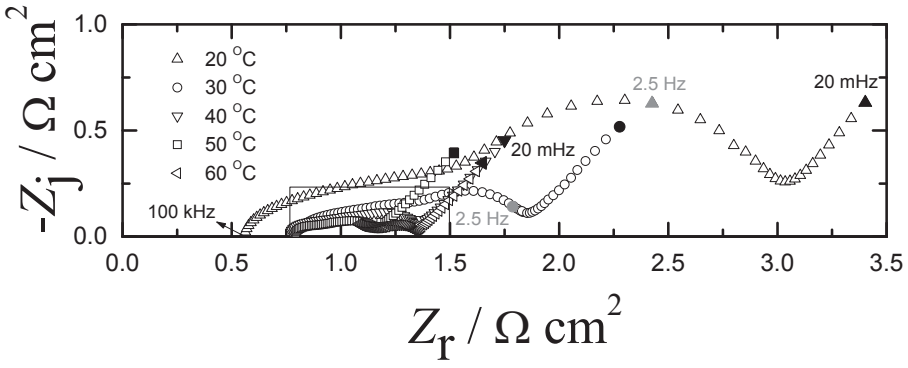

A

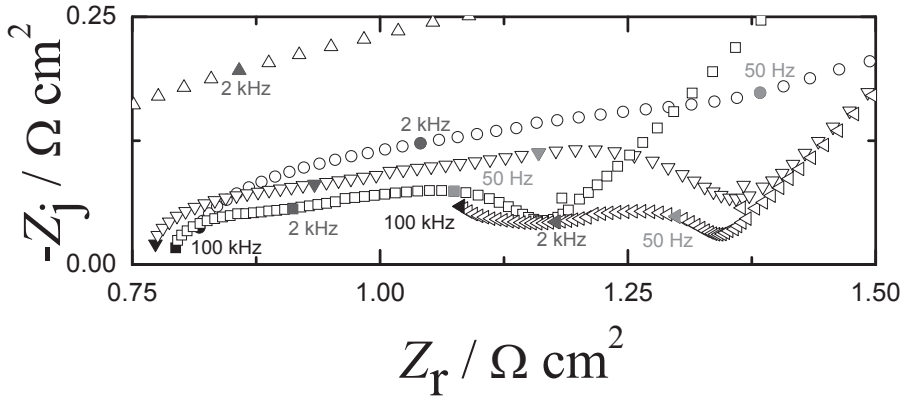

B

Figure 5-17. Impedance response in Nyquist format for a $LiCoO_2$|C coin cell under 4 V cell potential with surrounding temperature, ranging from 20 to 60 °C, as a parameter: A) complete spectra and B) low impedance values corresponding to the box in (A).

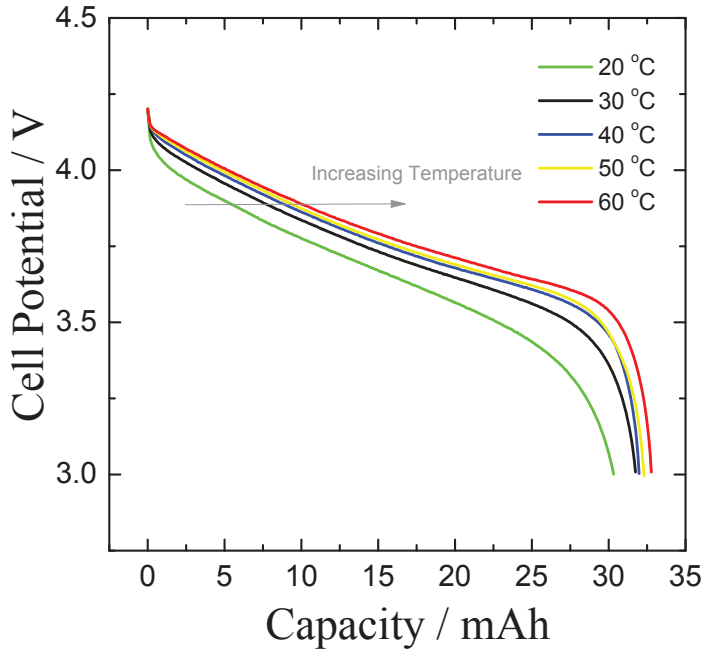

Figure 5-18. Discharge capacity of a $LiCoO_2$|C coin cell with the temperature, ranging from 20 to 60 °C, as a parameter. Discharge was at a constant 30 mA current (nominally a 1C rate).

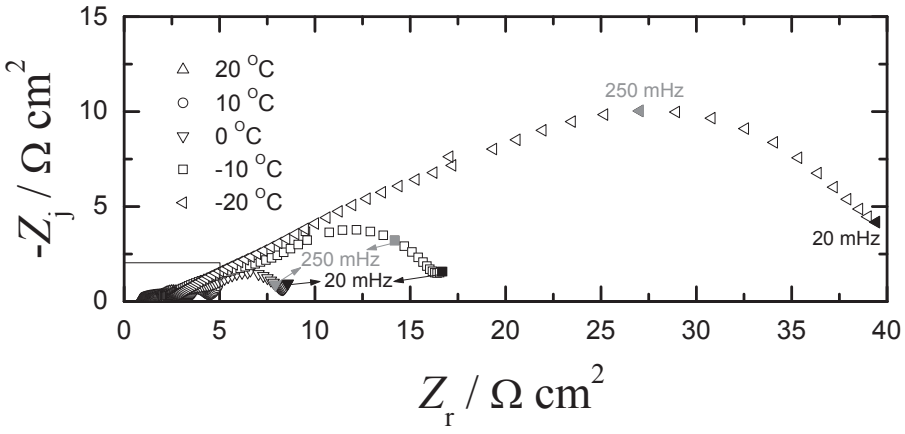

A

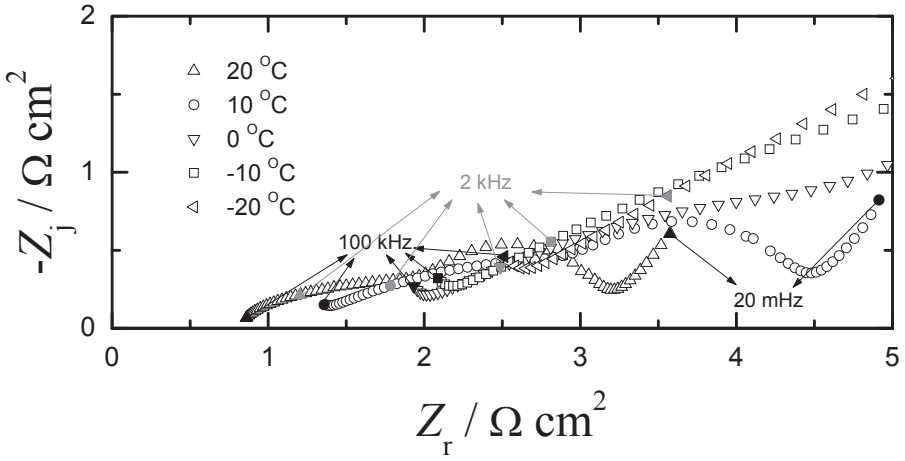

B

Figure 5-19. Impedance response in Nyquist format for a $LiCoO_2$|C coin cell under 4 V cell potential with surrounding temperature, ranging from 20 to -20 °C, as a parameter: A) complete spectra and B) high frequency values corresponding to the box in (A).

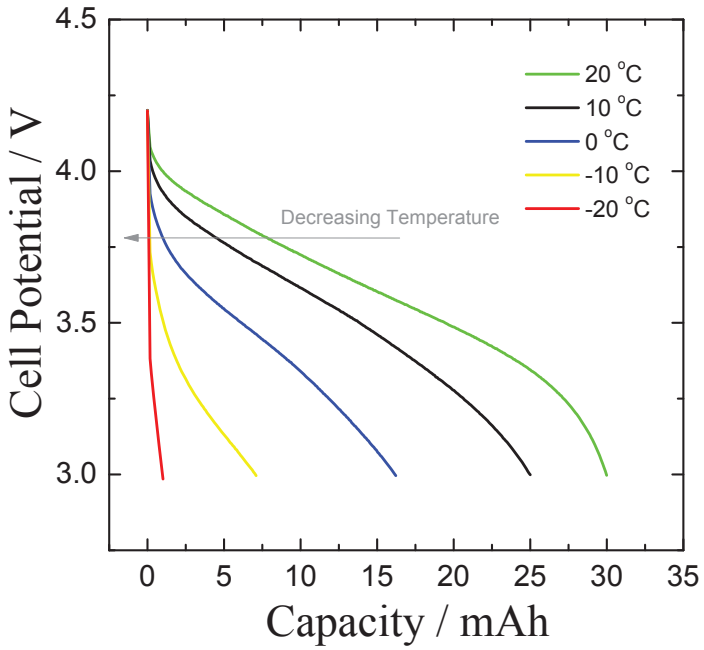

Figure 5-20. Discharge capacity of a $LiCoO_2$|C coin cell with the temperature, ranging from 20 to -20 °C, as a parameter. Discharge was at a constant 30 mA current (nominally a 1C rate).

CHAPTER 6
MATHEMATICAL MODELING

Two types of model were developed to interpret the $LiCoO_2$|C battery cell system: a measurement model and a process model. The high-frequency part of the impedance data is analyzed the measurement model. On the other hand, both high and low frequency parts of the data is described by the proposed process model.

6.1 Measurement Model Analysis

A measurement model analysis was employed to extract physically meaningful parameters. A graphical analysis was used to show that the change in the impedance response with over-discharging was due to a change in the ohmic resistance.

6.1.1 Measurement Model

The measurement model method for distinguishing between bias and stochastic errors is based on using a generalized model as a filter for non-replicacy of impedance data [37]. The measurement model is composed of a superposition of line-shapes which can be arbitrarily chosen subject to the constraint that the model satisfies the Kramers–Kronig relations. The model composed of Voigt elements in series with a solution resistance, shown in Figure 6-1 and described mathematically by

$$Z = R_0 + \sum_{k=1}^{n} \frac{R_k}{1 + j\omega R_k C_k} \tag{6–1}$$

has been shown to be a useful measurement model. With a sufficient number of parameters, the Voigt model was able to provide a statistically significant fit to a broad variety of impedance spectra [38].

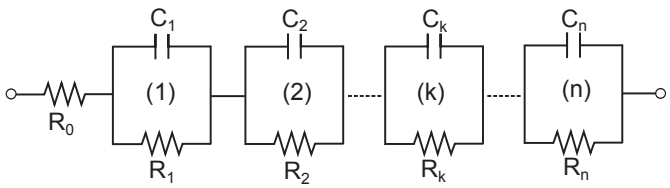

Figure 6-1. A schematic representation of the measurement model used by Agarwal et al. [38–40]

The measurement model was used first to filter lack of replication of repeated impedance scans. The statistics of the residual errors yielded an estimate for the variance (or standard deviation) of stochastic measurement errors [39]. This experimentally-determined variance was then used to weight subsequent regression of the measurement model to determine consistency with the Kramers–Kronig relations [40, 41]. This work was predicated on the assumption that, if the data can be represented by a model that is itself consistent with the Kramers–Kronig relations, the data can be considered to be consistent. The use of an experimental determination of the stochastic error structure allowed formal quantification of the extent of agreement with the Kramers–Kronig relations.

6.1.2 Measurement Model Results

The error analysis approach was applied to electrochemical impedance data collected for the Li-ion batteries. The experimental data was evaluated for the consistency with the Kramers–Kronig relations, using the experimentally determined variance to weight the regression of the measurement model. For measurements at normal operating potentials, the results at frequencies higher than 25 kHz were found to be inconsistent with the Kramers–Kronig relations. For the system subjected to overcharge to 5 V, subsequent measurements at a lower voltage were consistent with the Kramers–Kronig relations, even at frequencies as high as 100 kHz. In all cases, the data collected at low frequencies (20 mHz) were found to be consistent with the Kramers–Kronig relations. This result was observed for systems undergoing obvious transient behavior, such as shown in Figures 5-6 and 5-12. The consistency of the low-frequency data with the Kramers–Kronig relations means that the system was changing sufficiently slowly that individual scans could be regarded as being stationary. Only the Kramers–Kronig-consistent data were used for subsequent analysis under the assumption that the truncated data were subject to artifact such as caused by wires or electronics.

Comparison of scaled impedance may be used to assess to the extent to which differences in impedance response may be attributed to changes in reaction chemistry.

This approach was used successfully by Baril et al. [42] to show that the temporal evolution of impedance for a magnesium alloy could be attributed to changes in coverage by an oxide layer rather than to changes in reaction chemistry. The use of scaled impedance requires robust estimates for the ohmic resistance and the zero-frequency asymptote. In the present case, the scaling was based on the size of the high-frequency capacitive loop. The measurement model was used to assess the high-frequency asymptote for the real part of the impedance. This term is the ohmic resistance (R_e) for the cell. A truncated data set was used to estimate the charge-transfer resistance (R_t) for the high-frequency capacitive loop. The concept of using the measurement model to identify limits was presented by Orazem et al. [43] for estimating the polarization resistance in corrosion studies.

The effect of overcharging and over-discharging can be demonstrated by plotting a scaled impedance in which $-Z_j/R_t$ is plotted as a function of $(Z_r - R_e)/R_t$. The results are presented in Figure 6-2A. Superposition of the scaled data was not possible, suggesting that the chemistry of the battery changed after overcharging. In contrast, as shown in Figure 6-2B, superposition was possible for scaled impedance results before and after over-discharge. The superposition of impedance curves shows that there were no mechanistic changes caused by over-discharge to a particular potential, for this case 2.2 V. The change in the impedance response after over-discharge can be attributed solely to a change in the ohmic resistance.

The results of the overcharge experiments are in agreement with the observations of Amatucci et al.,[44] who, based on x-ray diffraction of overcharged $LiCoO_2$ cathode materials, suggested that the cathode crystal structure collapses upon overcharge due to excess removal of lithium ions between CoO_2 layers. Thus, some of the lithium ions in the $LiCoO_2$ cathode are required to maintain the proper structural stability and oxidation state of the CoO_2 lattice. Under overcharge, these are removed, resulting in either a phase transition to a different CoO_2 morphology or breaking bonds that never properly heal.

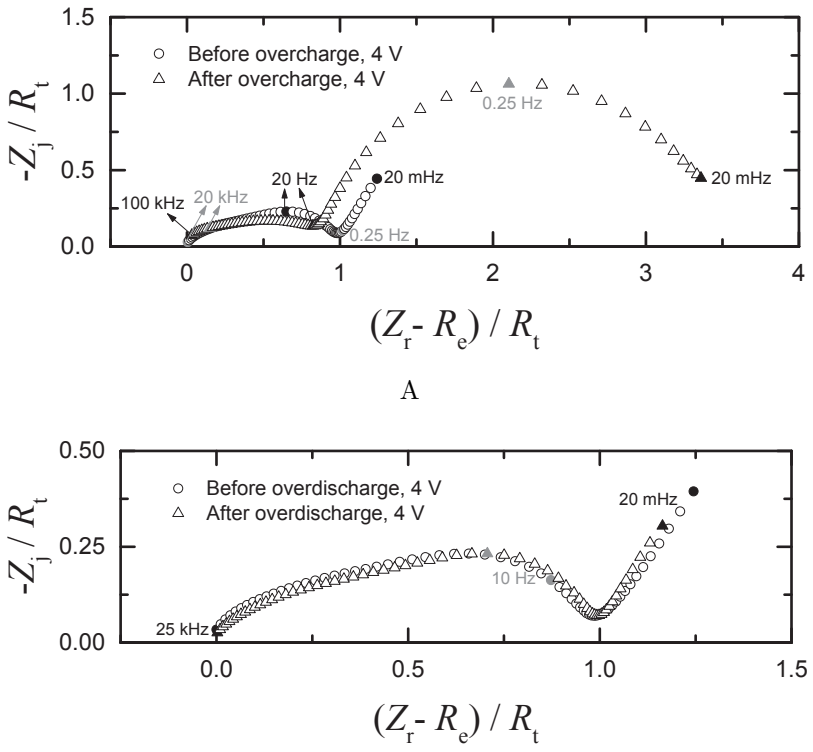

Figure 6-2. Scaled impedance result of a $LiCoO_2$|C cell at 4 V; A) before and after the cell was overcharged (see Figure 5-7) and B) before and after the cell was over-discharged (see Figure 5-13). Taken from Erol et al. [35]

This change is also seen in SEM pictures of the cathode in Figures 5-15C and 5-15D in comparison to Figures 5-15A and 5-15B. The observation that the voltage recovers (Figure 5-5), but not the impedance (Figure 6-2A), may be attributed to the sensitivity of impedance to transport and kinetic limitations.

The over-discharge results imply a source for extra lithium ions, which may be the solid electrolyte interphase (SEI) layer at the anode/electrolyte interface. This hypothesis is consistent with the transient change in the impedance. The observation that the open-circuit potential (Figure 5-11) and impedance response from the layer (Figure 6-2B) recovered under open-circuit conditions is notable, as this healing occurred without cell cycling. It is possible that the lowest value of over-discharge potential in the present work was not sufficiently low to cause irreversible damage. Maleki and Howard [5]

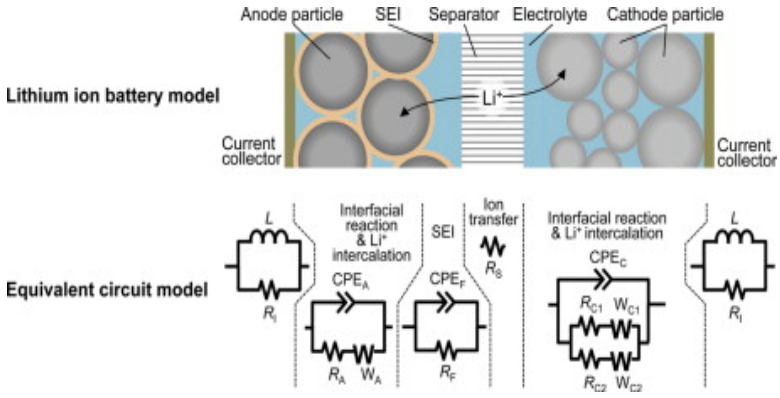

Figure 6-3. Equivalent circuit model for Li-ion batteries designed by Osaka et al. [9]

over-discharged the Li-ion batteries to lower potentials and observed a capacity fade for their batteries.

6.2 Process Model Development

The impedance data was partly modelled by the measurement model analysis. However, the availability of an accurate mathematical model of impedance and capacity loss could significantly accelerate battery development. Such a model can be used to enable lifetime prediction, to diagnose failure mechanisms, to design aging protocols, and to reduce degradation through materials design and system optimization. In order to reach these goals, it is essential for the model to be based on the underlying battery mechanics and physics of degradation, rather than the simple fitting of empirical circuit models. [45]

Osaka et al. [9] proposed an equivalent circuit model with an inductive component, an anode reaction, transport through the SEI, a cathode reaction, and diffusion of lithium ion as shown in Figure 6-3. Their model considered the components of the battery impedance to be in series. The Warburg impedances and the charge-transfer resistances corresponding to the different particle sizes were in parallel at the cathode. Their treatment of diffusion at the cathode allowed the model to fit the apparent Warburg response at low frequencies that showed a slope that was greater than 45 degrees. Li et al. [10] developed an electrochemistry-based impedance model for Li-ion batteries. The resulting model, which has anode and cathode impedances connected in series, is presented

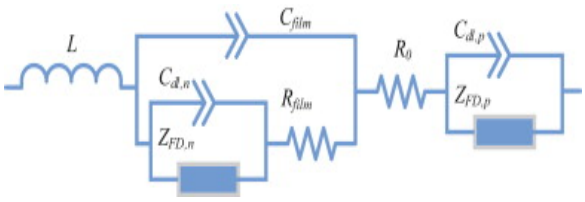

Figure 6-4. Equivalent circuit model for Li-ion batteries developed by Li et al. [10].

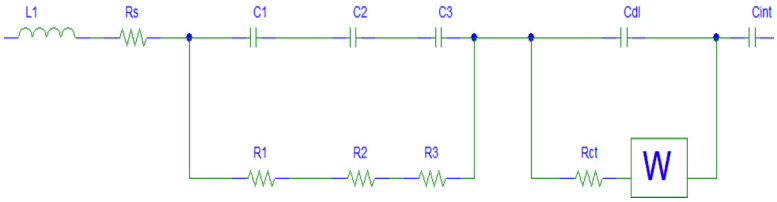

Figure 6-5. Equivalent circuit model for Li-ion batteries proposed by Gomez et al. [11]

in Figure 6-4. Their model has an inductor, separate CPE elements for the anode and SEI, and porous electrode behavior for the cathode. The fit looks good at high frequencies but it deviates at low frequencies. Gomez et al. [11] proposed an equivalent circuit model (shown in Figure 6-5) with an inductor, an ohmic resistance, R-C units in parallel to describe the slow migration of lithium ions through surface films of the electrode, a charge transfer resistance and a double layer capacitance of electrodes, Warburg impedance of the anode and cathode, and intercalation capacitance to denote the accumulation and depletion of lithium ions within the electrode and to show the variation of open circuit potential with SOC. Numerical values for C1, C2, and C3 and for R1, R2, and R3 cannot be obtained as only an effective capacitance and resistance can be extracted by regression. The intercalation capacitance placed in series does not account for the low-frequency part of a Li-ion battery impedance which is associated with lithium ion diffusion. Greenleaf et al. [12] used a similar equivalent circuit model including an inductance to cover very high frequency part and an intercalation capacitance in series with a Randles circuit to explain the low-frequency impedance. Their model is presented in Figure 6-6.

For the present work, an expression for the process model was developed based on battery dynamics, including the charge transfer reactions proposed to take place at the

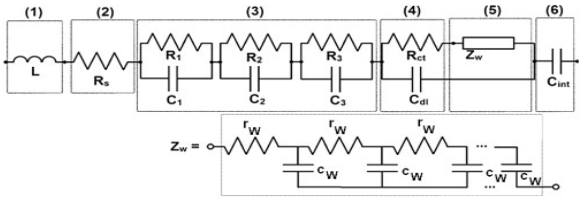

Figure 6-6. Equivalent circuit model for Li-ion batteries proposed by Greenleaf et al. [12]

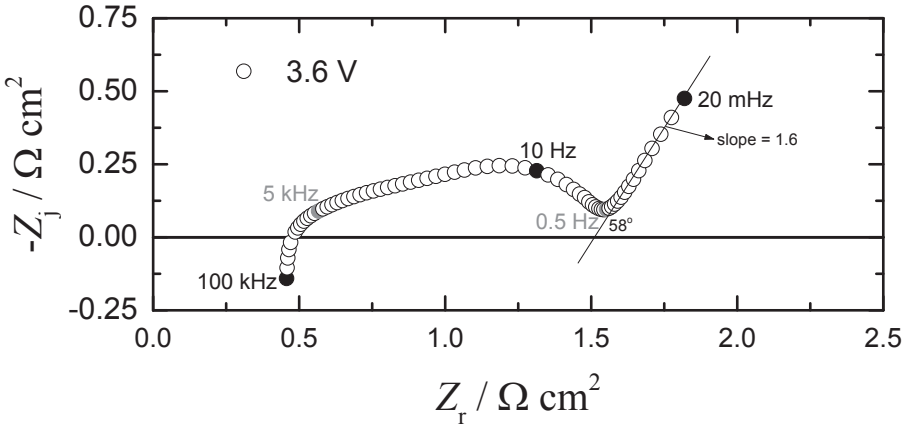

Figure 6-7. Typical impedance response of a $LiCoO_2$|C coin cell at a potential of 3.6 V, obtained from the present work.

cathode and anode, e.g. for $LiCoO_2$|C:

$$LiCoO_2 \rightleftharpoons Li_{1-x}CoO_2 + xLi^+ + xe^- \tag{6–2}$$

and

$$xLi^+ + xe^- + 6C \rightleftharpoons Li_xC_6 \tag{6–3}$$

respectively and lithium diffusion occuring in electrodes.

The impedance data obtained under normal operation conditions, e.g., at 3.6 V, revealed a depressed capacitive loop at high and intermediate frequencies and a straight line at low frequencies with slope greater than 45° as shown in Figure 6-7. The impedance data could not be described simply by a Randles circuit design (see Figure 3-2) because the high-frequency loop is not a perfect semicircle or suppressed semicircle (CPE behavior with one time constant) in a Nyquist plot, and the slope of the low-frequency

impedance is near 58°, which is much larger than the 45° associated with the Warburg impedance.

The Li-ion battery dynamics could not be examined by a simple equivalent electrical circuit representation due to the complex mechanisms inside battery. The impedance contribution of all components in the battery is needed to be taken into account separately to understand these mechanisms.

6.2.1 Anode

6.2.1.1 Cycling and SEI formation

Cycle life has a very great importance in applications of rechargeable batteries, but lifetime prediction is mostly based on empirical trends, rather than mathematical models. In practical Li-ion batteries, capacity fade occurs after many cycles, limited by slow electrochemical processes, such as the formation of a solid-electrolyte interphase (SEI) in the negative electrode, which correlates with reversible lithium intercalation process. The SEI layer is a passivating film that forms at the surface of the active electrode material in the battery, protecting the electrolyte and other battery components (especially graphitic anode) from undesirable reactions.

The most common source of capacity fade in Li-ion batteries is the loss of lithium due to the SEI formation at the negative electrode during charging. SEI formation first protects the electrode against solvent decomposition; however, over time it causes a continuous capacity fade as the SEI layer thickens. A large variety of compounds has been observed in this layer. [45, 46]

The desired electrochemical reaction is the intercalation of lithium, but lithium can also react with components of the electrolyte to form a solid-electrolyte interphase. Figure 6-8A provides a schematic diagram of the competing reactions in SEI and graphitic anode. Deshpande et al. [47] suggested that the cracks at the graphite particle surface propagate upon electrochemical cycling. For each cycle, the newly cracked surface is exposed to electrolyte and thus results in SEI formation. Figure 6-8B shows that as a

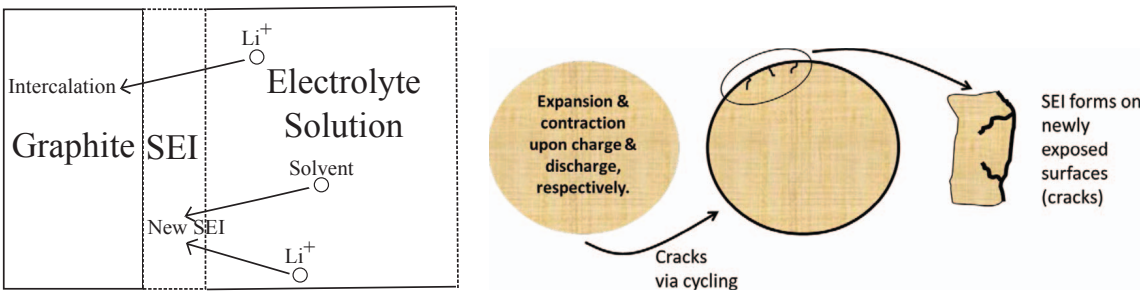

A B

Figure 6-8. Solid-electrolyte interphase formation during electrochemical cycling; A) on the graphite anode (mechanism); adapted from Pinson and Bazant [45], B) on a lithiated graphite particle due to diffusion induced stresses; taken from Deshpande et al. [47]

result of diffusion induced stresses, the cracks at the particle surface propagate with cycling, new surface is exposed to electrolyte, and Li is consumed in the formation of new SEI. Aurbach et al. [48] explains that the lithiation of graphite process during cycling changes the particle orientation due to cracking. It allows solution species to penetrate between graphite particles, and therefore isolate them electrically from the bulk electrolyte. This cracking and the formation of SEI can be seen on the SEM images shown in Figure 5-16.

The SEI formation theory and the cracking process suggests that the impedance model on the anode and the SEI layer would be in a current addition form since the lithium intercalation and the SEI formation occur in parallel reactions. In other words, the anodic and the SEI impedances should be in parallel rather than in series in the equivalent circuit design.

6.2.1.2 Linear diffusion in anode

A slow diffusion of the reacting species through the graphite [49] and large particle sizes in the electrode [50] imply a linearized diffusion model in a semi-infinite planar domain which is Warburg-type diffusion impedance.

6.2.2 Electrolyte and Separator

Under the assumption that the concentrations are uniform within the electrolyte, the passage of current through the system is controlled by the ohmic resistance. [27] Thus, an ohmic resistance (R_e) plays a role due to the ion transfer in the electrolyte through the separator.

6.2.3 Cathode

6.2.3.1 Anomalous diffusion in cathode

A characteristic feature of the impedance response of the $LiCoO_2$|C battery is the slope of the straight line, seen at low frequencies in the Nyquist plot, that is greater than 45 degrees. This behavior is not seen for all lithium battery chemistries. Greenleaf et al. [12] show that the $LiFePO_4$ system yields a slope of 45 degrees, which is consisted with Fickian diffusion impedance. Osaka et al. [9] suggest that the larger slope can be attributed to diffusion to particles of different sizes. In the present work, an alternative explanation is posed in terms of anomalous diffusion.

Ordinary diffusion which obeys Fick's second law is characterized by the linear time dependence of a mean squared displacement (MSD) expressed as

$$< r^2(t) > \sim t \tag{6–4}$$

where r is the displacement of the diffusion species after the time t. However, if the MSD does not obey equation 6–4 due to obstacles, time delays, or particle interactions, the diffusion will have a power-law dependence on t given as

$$< r^2(t) > \sim t^{\gamma} \tag{6–5}$$

where γ is the anomalous diffusion exponent ($\gamma \neq 1$), the processes are termed anomalous diffusion, which no longer follows Fick's second law. When $\gamma < 1$ the process is called sub-diffusive and when $\gamma > 1$ it is super-diffusive.[51, 52] In sub-diffusion case, the

constitutive equation differs from ordinary diffusion, being

$$J = -D\frac{\partial^{1-\gamma}}{\partial^{1-\gamma}t}\frac{\partial c}{\partial x} \tag{6–6}$$

where J is the flux, D is the diffusion coefficient, and $\partial c/\partial x$ is the concentration gradient. This constitutive equation is derived from continuous time random walk in the macroscopic limit. The random walkers wait after each jump for a period of time drawn from a broad power-law distribution. The effect is that some particles remain stuck for a long time and diffusion is slower. The impedance for this type of anomalous diffusion was used which is associated with systems that show a diffusion hindered by sporadic adsorption of diffusing species to a fixed substrate; in this particular case $LiCoO_2$ cathode. The associated impedance response, with a reflecting boundary condition, was solved by Bisquert and Compte [53]. The resulting diffusion impedance is expressed as

$$Z_{\mathrm{d}}(\omega) = \frac{Z_{\mathrm{d}}(0)}{\tau^{\gamma/2}}\coth\left[(\mathrm{j}\omega\tau)^{\gamma/2}\right] \tag{6–7}$$

where $Z_{\mathrm{d}}(0)$ is the zero-frequency asymptote for the real part of the diffusion impedance, and τ is the time constant. In the high-frequency limit, the impedance is proportional to $Z_{\mathrm{d}}(0)/\tau^{\gamma/2}$. [27]

6.2.4 Process Model Results

The equivalent circuit representation of the model developed in the present work for the battery system is shown in Figure 6-9. The resulting model can be expressed as

$$Z = Z_{\mathrm{a||S}} + R_{\mathrm{e}} + Z_{\mathrm{c}} \tag{6–8}$$

where $Z_{\mathrm{a||S}}$ is the impedance corresponding to the anode and the SEI layer and given as

$$Z_{\mathrm{a||S}}(\omega) = \frac{(R_{\mathrm{t,a}} + Z_{\mathrm{d,a}})R_{\mathrm{t,S}}}{R_{\mathrm{t,a}} + Z_{\mathrm{d,a}} + \mathrm{j}\omega(R_{\mathrm{t,a}} + Z_{\mathrm{d,a}})R_{\mathrm{t,S}}C_{\mathrm{a||S}}} \tag{6–9}$$

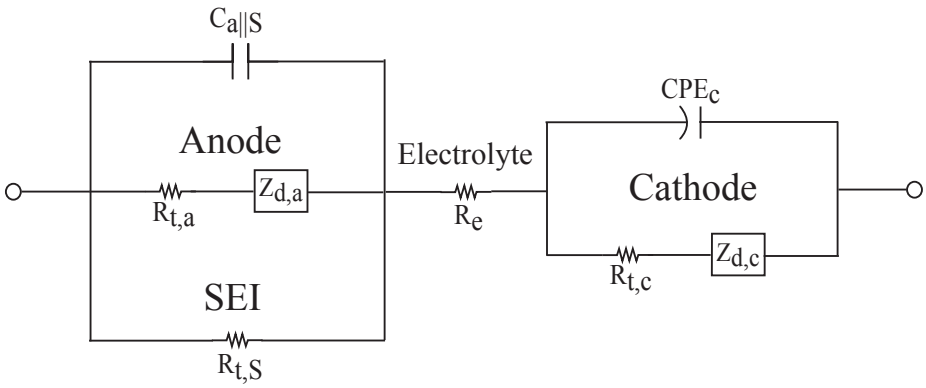

Figure 6-9. Equivalent circuit representation of the model developed in the present work for the complete Li-ion battery system.

The diffusion impedance for the anode, $Z_{\mathrm{d,a}}$ is simply a Warburg impedance,

$$Z_{\mathrm{d,a}} = \frac{A_{\mathrm{W,a}}}{\sqrt{\mathrm{j}\omega}} \tag{6–10}$$

where $A_{\mathrm{W,a}}$ is the Warburg impedance coefficient, and Z_{c} is the cathodic impedance expressed as

$$Z_{\mathrm{c}}(\omega) = \frac{R_{\mathrm{t,c}} + Z_{\mathrm{d,c}}}{1 + (\mathrm{j}\omega)^{\alpha_{\mathrm{c}}}(R_{\mathrm{t,c}} + Z_{\mathrm{d,c}})Q_{\mathrm{c}}} \tag{6–11}$$

As the measured frequency range does not reveal the sharp increase associated with the reflecting boundary condition, an asymptotic form of their expression was used, with the resulting diffusion impedance ($Z_{\mathrm{d,c}}$) given as

$$Z_{\mathrm{d,c}}(\omega) = \frac{A_{\mathrm{d,c}}}{(\mathrm{j}\omega)^{1-\gamma_{\mathrm{d,c}}/2}} \tag{6–12}$$

where $A_{\mathrm{d,c}}$ is a lumped parameter

$$A_{\mathrm{d,c}} = \frac{Z_{\mathrm{d,c}}(0)}{\tau_{\mathrm{d,c}}^{\gamma_{\mathrm{d,c}}/2}} \tag{6–13}$$

containing the diffusion time constant, $\tau_{\mathrm{d,c}}$

$$\tau_{\mathrm{d,c}} = \frac{\delta_{\mathrm{d,c}}^2}{D_{\mathrm{d,c}}} \tag{6–14}$$

and the zero-frequency asymptote for the real part of the diffusion impedance, $Z_{\mathrm{d,c}}(0)$.

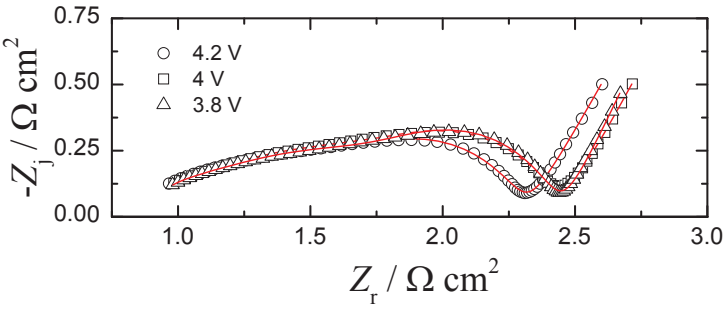

A

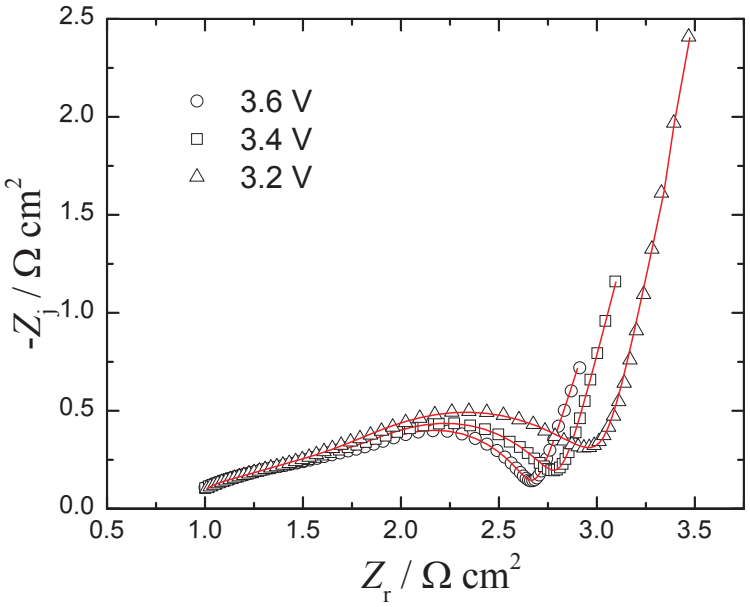

B

Figure 6-10. Impedance response a $LiCoO_2$|C coin cellat a temperature of 20 °C with cell potential as a parameter: A) potential ranging from 4.2 to 3.8 V; B) potential ranging from 3.6 to 3.2 V. The line represents a fit of equation 6–8 to that data.

The regression results are presented in Figure 6-10A for a cell potential ranging from 4.2 to 3.8 V and in Figure 6-10B for a cell potential ranging from 3.6 to 3.2 V. As seen in Figure 6-10, the quality of the fits are excellent. The fitting parameters obtained by using the Levenberg-Marquardt regression analysis are shown in Tables 6-1 and 6-2, where regressed values of the parameters are provided with their $\pm\sigma$ confidence intervals.

The regression results are presented in Figure 6-11A for a cell temperature ranging from 10 to 20 °C and Figure 6-11B for a cell potential ranging from 30 to 50 °C. As seen

Table 6-1. Regression results and $\pm\sigma$ confidence intervals of a fit of equation 6–8 to the data for cell potential ranging from 4.2 to 3.8 V at a temperature of 20 °C. The potential range of 3.6-3.2 V is shown in Figure 6-2.

Parameter	4.2 V	4 V	3.8 V
$C_{a\|\|S}$ / μF cm^{-2}	39±2.8	41±2.5	44±4.4
$A_{W,a}$ / Ω cm^2 s$^{-0.5}$	53±1.4	51±1.1	47±1.5
$R_{t,a}$ / Ω cm^2	0.173±0.0084	0.180±0.0069	0.180±0.010
$R_{t,S}$ / Ω cm^2	1.10±0.019	1.19±0.018	1.17±0.022
R_e / Ω cm^2	0.874±0.0053	0.894±0.0048	0.893±0.0077
$R_{t,c}$ / Ω cm^2	0.36±0.021	0.39±0.019	0.40±0.023
α_c	0.91±0.015	0.92±0.014	0.96±0.018
Q_c / F cm^{-2} s$^{\alpha_c-1}$	0.0335±0.00066	0.0333±0.00061	0.0375±0.0011
$\gamma_{d,c}$	0.644±0.0054	0.617±0.0043	0.551±0.0099
$A_{d,c}$/ Ω cm^2 s$^{-\gamma_{d,c}/2}$	0.1382±0.00093	0.1821±0.00098	0.112±0.0013

Table 6-2. Regression results and $\pm\sigma$ confidence intervals of a fit of equation 6–8 to the data for cell potential ranging from 3.6 to 3.2 V at a temperature of 20 °C. The potential range of 4.2-3.8 V is shown in Figure 6-1.

Parameter	3.6 V	3.4 V	3.2 V
$C_{a\|\|S}$ / μF cm^{-2}	63±2.4	68±2.4	64±5.1
$A_{W,a}$ / Ω cm^2 s$^{-0.5}$	35.9±0.57	34.0±0.57	37.1±1.3
$R_{t,a}$ / Ω cm^2	0.197±0.0044	0.198±0.0043	0.177±0.0097
$R_{t,S}$ / Ω cm^2	1.15±0.012	1.12±0.015	0.94±0.025
R_e / Ω cm^2	0.940±0.0030	0.945±0.0027	0.949±0.0056
$R_{t,c}$ / Ω cm^2	0.61±0.012	0.77±0.016	1.21±0.029
α_c	0.930±0.0067	0.869±0.0062	0.755±0.0076
Q_c / F cm^{-2} s$^{\alpha_c-1}$	0.0527±0.00058	0.0560±0.00061	0.0556±0.00092
$\gamma_{d,c}$	0.379±0.0045	0.311±0.0032	0.247±0.0039
$A_{d,c}$/ Ω cm^2 s$^{-\gamma_{d,c}/2}$	0.1374±0.00068	0.2060±0.00069	0.407±0.0014

in Figure 6-11, the quality of the fits are excellent. The fitting parameters are shown in Tables 6-3 and 6-4.

The regressed values of the anodic-SEI capacitance ($C_{a||S}$) are shown in Figure 6-12 as functions of cell potential and temperature. The anodic-SEI capacitance is smaller at the 4.2-3.8 V potential range than 3.6-3.2 V potential range (shown in Figure 6-12A); while, $C_{a||S}$ increases exponentially as temperature increases (shown in Figure 6-12B).

The regressed values of the anodic Warburg impedance coefficient ($A_{W,a}$) are shown in Figure 6-13 as functions of cell potential and temperature. The anodic Warburg impedance coefficient is larger at 4.2-3.8 V potential range than 3.6-3.2 V potential range

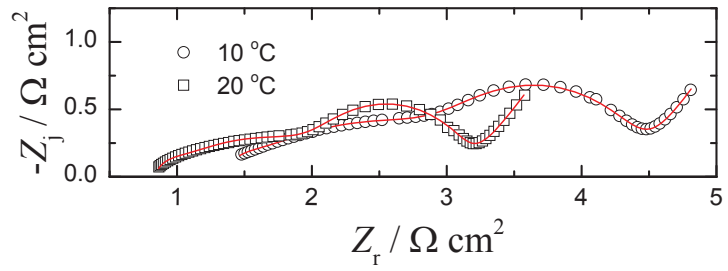

A

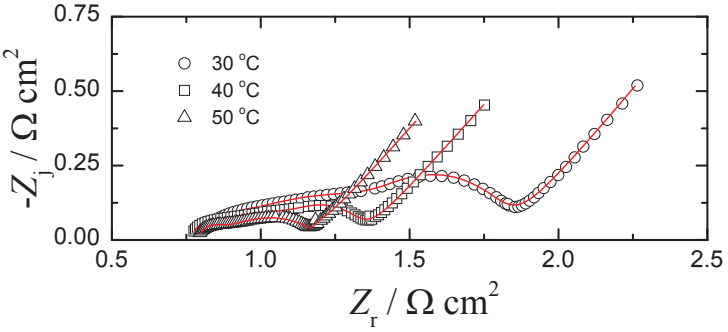

B

Figure 6-11. Impedance response a $LiCoO_2$|C coin cell at a potential of 4 V with cell temperature as a parameter: A) temperature ranging from 10 to 20 °C; B) temperature ranging from 30 to 50 °C. The line represents a fit of equation 6–8 to that data.

Table 6-3. Regression results and $\pm\sigma$ confidence intervals of a fit of equation 6–8 to the data for cell temperature ranging from 10 to 20 °C at a potential of 4 V. The temperature range of 30-50 °C is shown in Figure 6-4.

Parameter	10 °C	20 °C
$C_{a\|\|S}$ / μF cm^{-2}	28±1.8	28.8±0.84
$A_{W,a}$ / Ω cm^2 s$^{-0.5}$	58.8±0.87	52.5±0.51
$R_{t,a}$ / Ω cm^2	0.256±0.0066	0.195±0.0045
$R_{t,S}$ / Ω cm^2	1.93±0.013	1.383±0.0073
R_e / Ω cm^2	1.357±0.0074	0.845±0.0022
$R_{t,c}$ / Ω cm^2	1.19±0.018	0.954±0.0094
α_c	0.912±0.0074	0.938±0.0052
Q_c / F cm^{-2} s$^{\alpha_c-1}$	0.0662±0.00088	0.0608±0.00065
$\gamma_{d,c}$	0.72±0.015	0.785±0.0087
$A_{d,c}$/ Ω cm^2 s$^{-\gamma_{d,c}/2}$	0.254±0.0042	0.203±0.0023

Table 6-4. Regression results and $\pm\sigma$ confidence intervals of a fit of equation 6–8 to the data for cell temperature ranging from 30 to 50 °C at a potential of 4 V. The temperature range of 10-20 °C is shown in Figure 6-3.

Parameter	30 °C	40 °C	50 °C
$C_{a\|\|S}$ / μF cm^{-2}	43±1.8	56±2.1	84±2.7
$A_{W,a}$ / Ω cm^2 s$^{-0.5}$	34.2±0.77	25.9±0.82	13.1±0.15
$R_{t,a}$ / Ω cm^2	0.138±0.0048	0.103±0.0035	0.097±0.0018
$R_{t,S}$ / Ω cm^2	0.73± 0.010	0.46±0.011	0.42±0.016
R_e / Ω cm^2	0.809±0.0020	0.767±0.0013	0.792±0.0011
$R_{t,c}$ / Ω cm^2	0.30±0.011	0.12±0.011	0.039±0.0017
α_c	0.98±0.016	0.99±0.020	1.00±0.01
Q_c / F cm^{-2} s$^{\alpha_c-1}$	0.054±0.0019	0.049±0.0035	0.013±0.0033
$\gamma_{d,c}$	0.886±0.0063	0.925±0.0039	0.944±0.0057
$A_{d,c}$/ Ω cm^2 s$^{-\gamma_{d,c}/2}$	0.209±0.0017	0.198±0.0010	0.172±0.0012

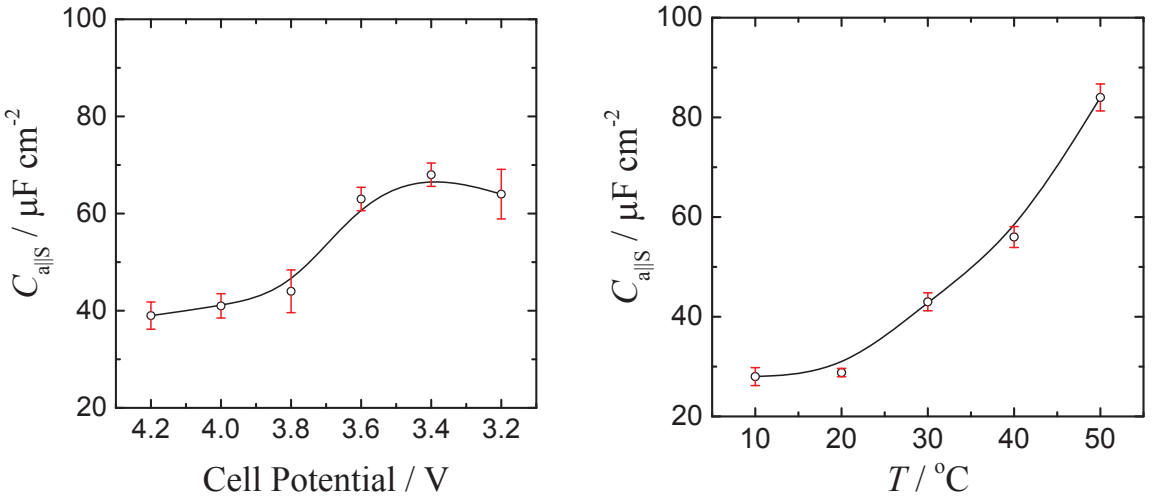

Figure 6-12. Regressed value of the anodic-SEI capacitance: A) as a function of potential at a temperature of 20 °C; B) as a function of temperature at a potential of 4 V. The line is a spline fit. Error bars represent the $\pm\sigma$ confidence intervals obtained from the regression.

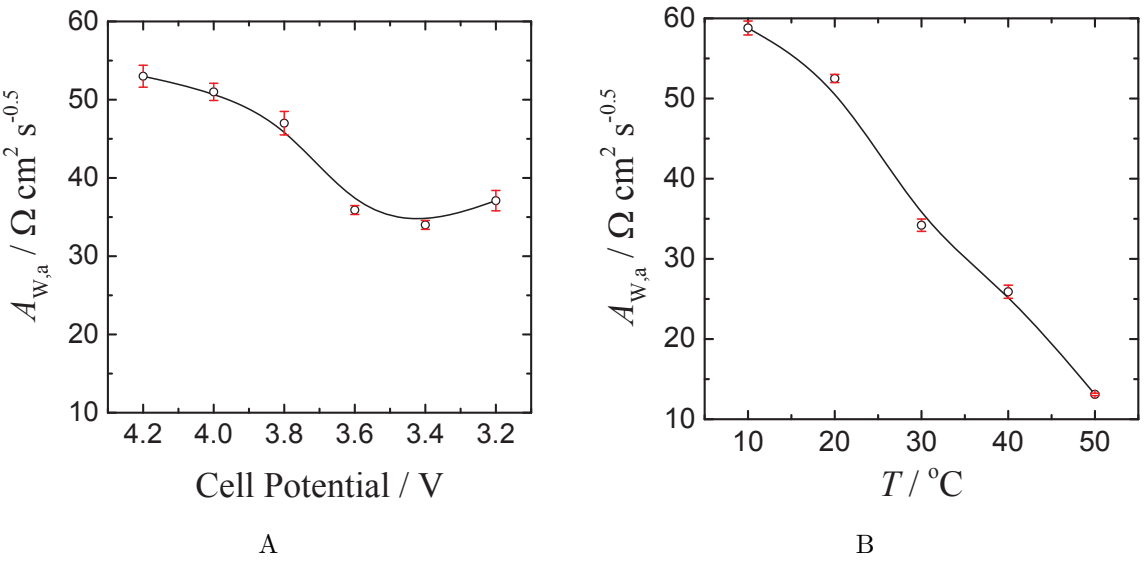

Figure 6-13. Regressed value of the anodic Warburg impedance coefficient: A) as a function of potential at a temperature of 20 °C; B) as a function of temperature at a potential of 4 V. The line is a spline fit. Error bars represent the $\pm\sigma$ confidence intervals obtained from the regression.

(shown in Figure 6-13A); while. $A_{W,a}$ decreases sharply as temperature rises (shown in Figure 6-13B).

The regressed values of the anodic charge-transfer resistance ($R_{t,a}$) as a function of cell potential and temperature are shown in Figure 6-14. The regressed values of the SEI charge-transfer resistance ($R_{t,S}$) as a function of cell potential and temperature are shown in Figure 6-15. The regressed values of the ohmic resistance (R_e) as a function of cell potential and temperature are shown in Figure 6-16. The regressed values of the cathodic charge-transfer resistance ($R_{t,c}$) as a function of cell potential and temperature are shown in Figure 6-17. All charge-transfer resistance values become smaller as the temperature increases, implying that the electrochemical reaction rate gets faster with increasing temperature as seen in Figures 6-14B, 6-15B, and 6-17B. On the other hand, the Ohmic resistance is higher only at 10 °C and roughly independent of temperature between 20 °C to 50 °C shown in Figure 6-16B. The cathodic charge transfer resistance decreases at

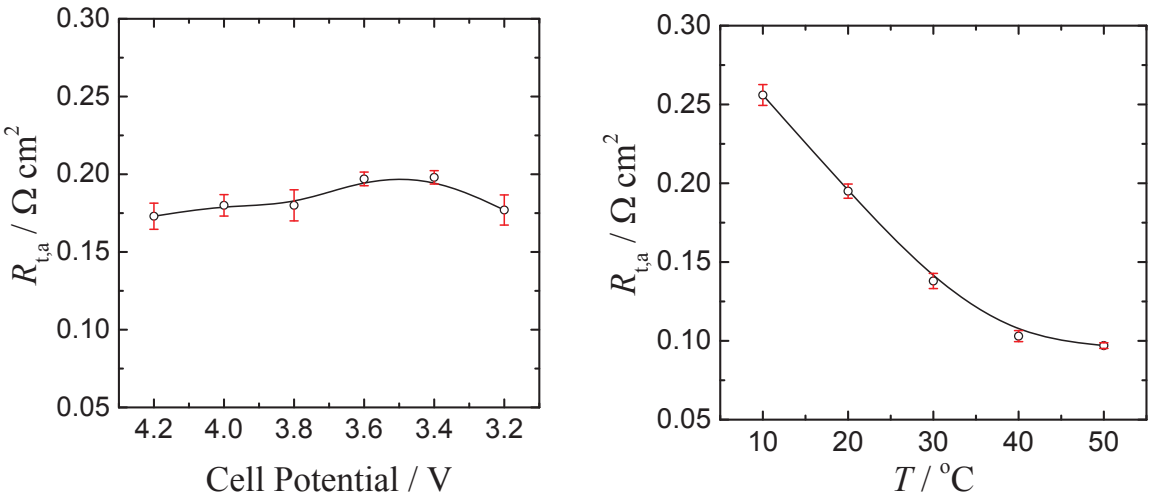

Figure 6-14. Regressed value of the anodic charge-transfer resistance: A) as a function of potential at a temperature of 20 °C; B) as a function of temperature at a potential of 4 V. The line is a spline fit. Error bars represent the $\pm\sigma$ confidence intervals obtained from the regression.

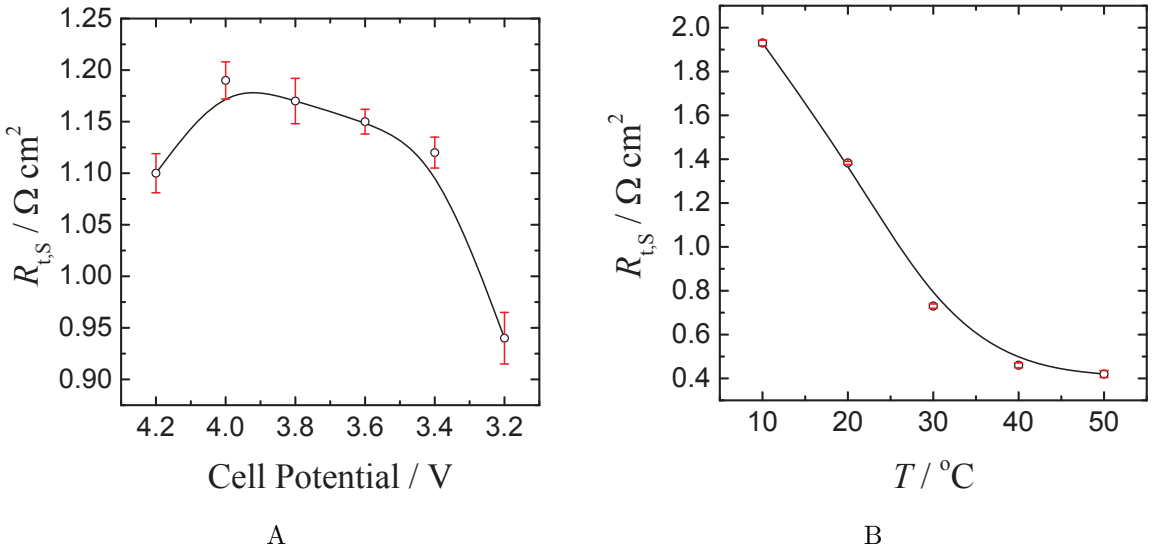

Figure 6-15. Regressed value of the SEI charge-transfer resistance: A) as a function of potential at a temperature of 20 °C; B) as a function of temperature at a potential of 4 V. The line is a spline fit. Error bars represent the $\pm\sigma$ confidence intervals obtained from the regression.

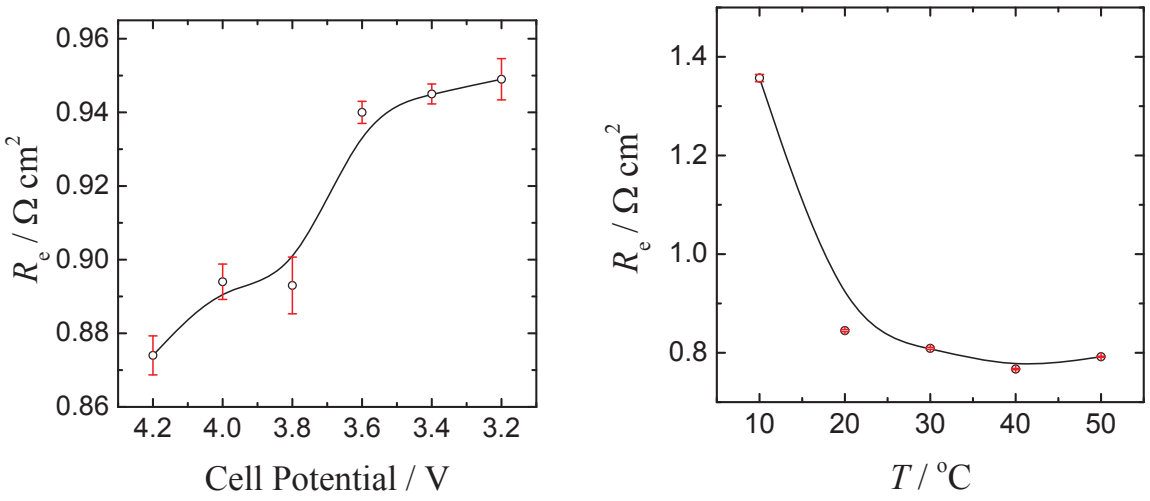

A B

Figure 6-16. Regressed value of the ohmic resistance: A) as a function of potential at a temperature of 20 °C; B) as a function of temperature at a potential of 4 V. The line is a spline fit. Error bars represent the $\pm\sigma$ confidence intervals obtained from the regression.

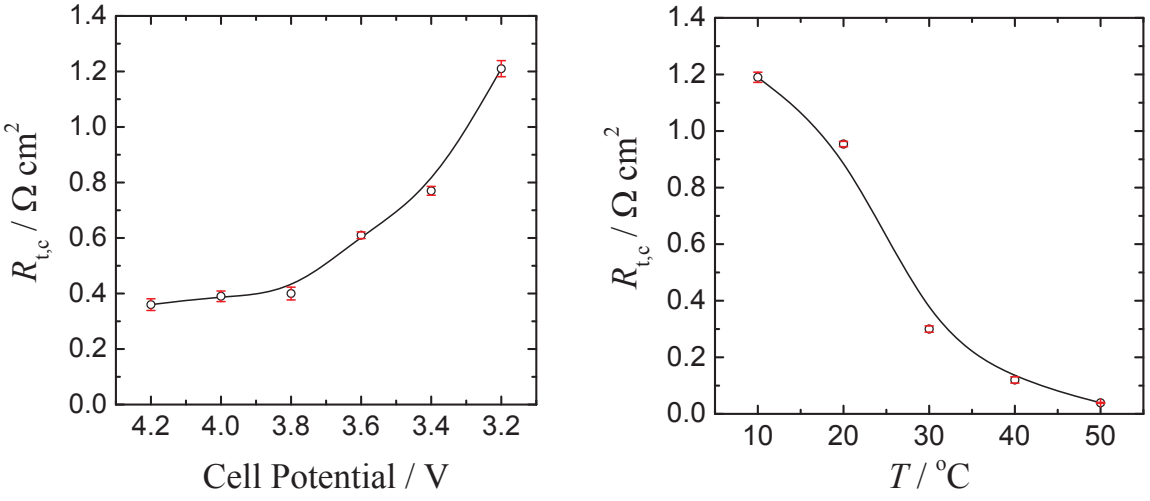

A B

Figure 6-17. Regressed value of the cathodic charge-transfer resistance: A) as a function of potential at a temperature of 20 °C; B) as a function of temperature at a potential of 4 V. The line is a spline fit. Error bars represent the $\pm\sigma$ confidence intervals obtained from the regression.

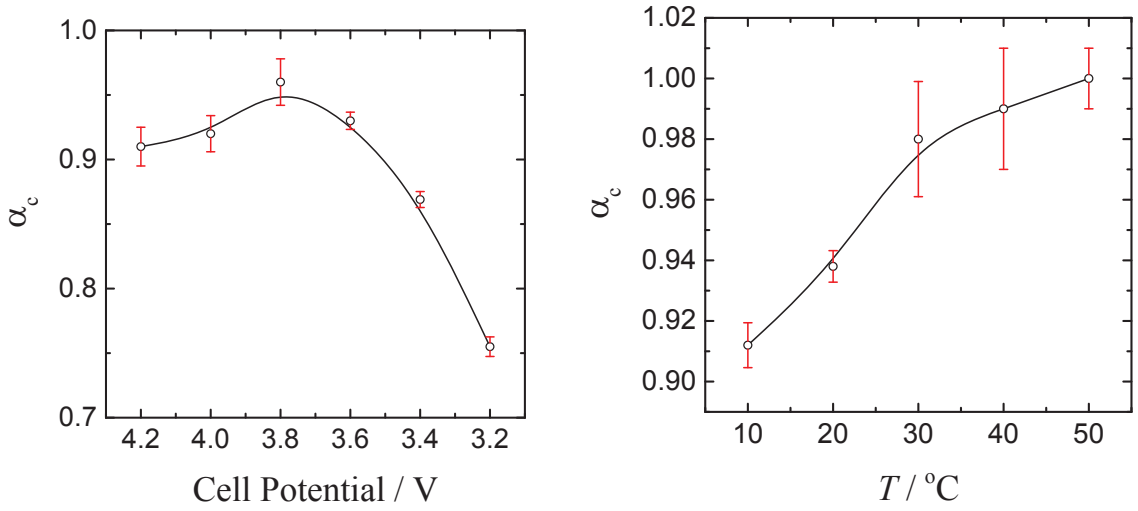

Figure 6-18. Regressed value of the cathodic CPE exponent: A) as a function of potential at a temperature of 20 °C; B) as a function of temperature at a potential of 4 V. The line is a spline fit. Error bars represent the $\pm\sigma$ confidence intervals obtained from the regression.

higher SOC; whereas, the other resistances ($R_{t,a}$, $R_{t,S}$, and R_e) change slightly, as seen in Figures 6-14A, 6-15A, 6-16A, and 6-17B.

The regressed values of the cathodic CPE exponent (α_c) as a function of cell potential and temperature are shown in Figure 6-18. As shown in Figures 6-18A and 6-18B, the CPE behavior disappears, and the system becomes more capacitive at upper SOC and at high temperature for Li-ion batteries.

The regressed values of the cathodic CPE coefficient (Q_c) are shown in Figure 6-19 as functions of cell potential and temperature. The cathodic CPE coefficient is slightly larger at low SOC than at high SOC (shown in Figure 6-19A), while it drops as temperature increases (shown in Figure 6-19B).

The regressed values of the cathodic anomalous diffusion exponent ($\gamma_{d,c}$) are shown in Figure 6-20 as functions of cell potential and temperature. As shown in Figures 6-20A and 6-20B, lithium ion diffusion gets stickier at low SOC and at low temperature. In other words, the diffusion becomes more Fickian at higher temperature and upper potentials.

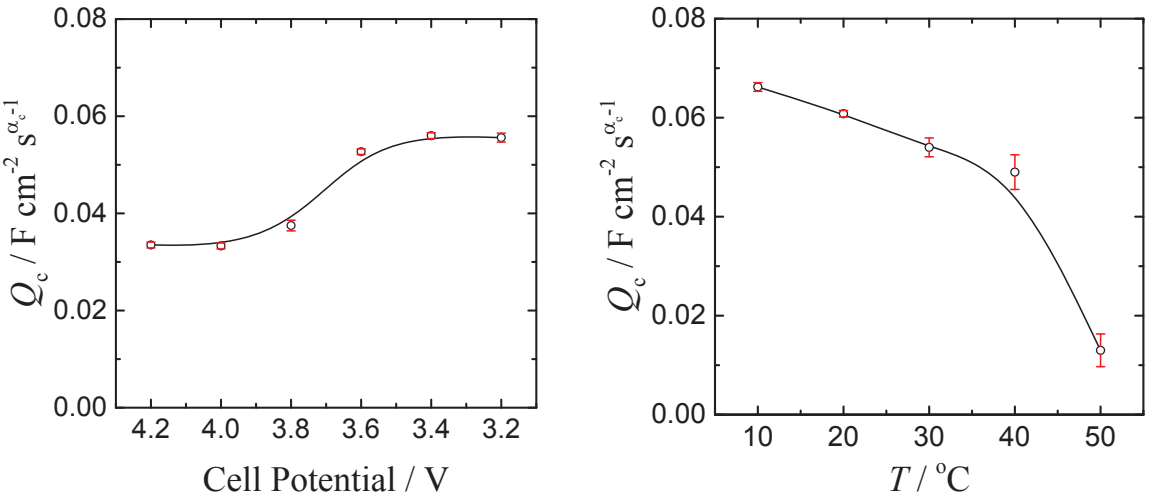

A B

Figure 6-19. Regressed value of the cathodic CPE coefficient: A) as a function of potential at a temperature of 20 °C; B) as a function of temperature at a potential of 4 V. The line is a spline fit. Error bars represent the $\pm\sigma$ confidence intervals obtained from the regression.

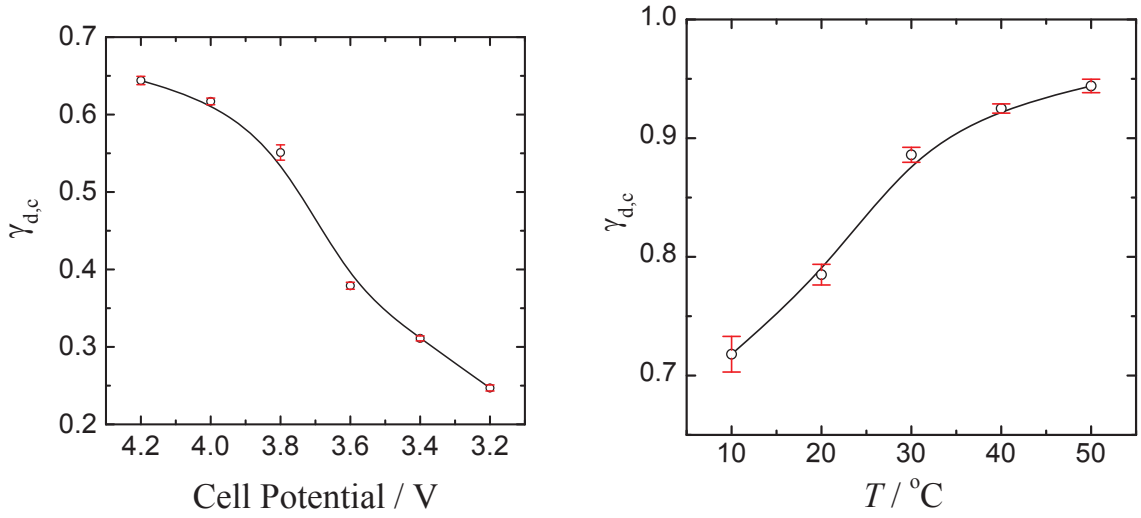

A B

Figure 6-20. Regressed value of the cathodic anomalous diffusion exponent: A) as a function of potential at a temperature of 20 °C; B) as a function of temperature at a potential of 4 V. The line is a spline fit. Error bars represent the $\pm\sigma$ confidence intervals obtained from the regression.

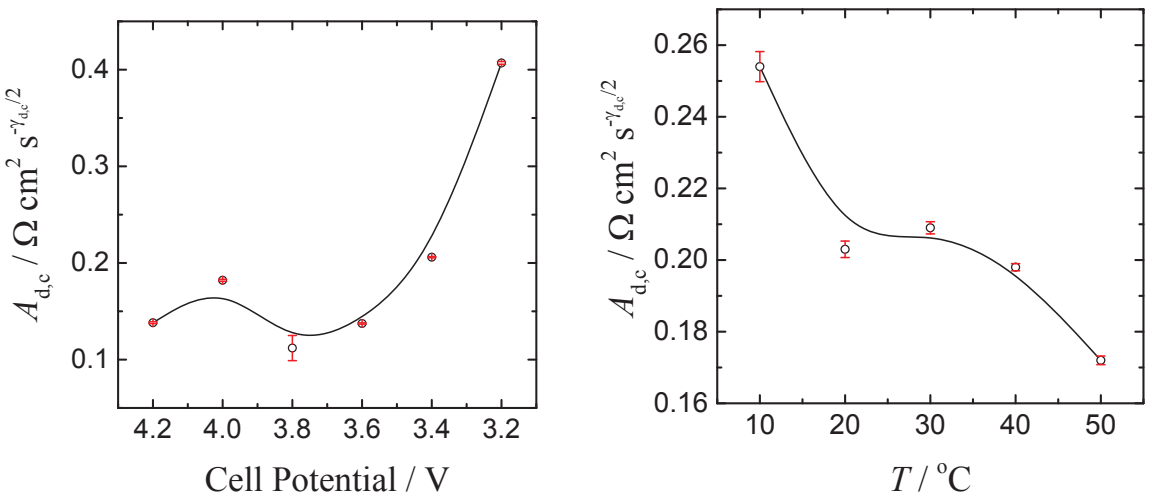

Figure 6-21. Regressed value of the cathodic anomalous diffusion lumped parameter: A) as a function of potential at a temperature of 20 °C; B) as a function of temperature at a potential of 4 V. The line is a spline fit. Error bars represent the $\pm\sigma$ confidence intervals obtained from the regression.

The regressed values of the cathodic anomalous diffusion lumped parameter ($A_{d,c}$) are shown in Figure 6-21 as functions of cell potential and temperature. This lumped parameter has the highest value at 3.2 V, while it is more independent of potential from 4.2 V to 3.4 V, as seen in Figure 6-21A. The term $A_{d,c}$ slightly changes at moderate temperatures (between 20 °C and 40 °C) shown Figure 6-21B. It is largest at 10 °C and the smallest at 50 °C. The analogous term of $A_{d,c}$ for ordinary diffusion at anode, $A_{W,a}$, has weak dependence on SOC and strong dependence on temperature. However, $A_{d,c}$ has strong dependence on SOC and weak dependence on temperature.

CHAPTER 7
CONCLUSIONS

The object of this work was to develop a new interpretation for the impedance response of $LiCoO_2$|C batteries in response to temperature extremes, overcharge, and over-discharge. Within the nominal operating range of potentials, 3-4.2 V, the impedance in Nyquist representations showed a high-frequency inductive feature, a broad mid-frequency capacitive loop, and a low-frequency straight line that had a slope greater than the 45 degree line expected for ordinary diffusion impedance. The magnitude of the impedance increased when the battery was over-discharged to 2.2 V and when the battery was overcharged to 5 V. Upon resting for 48 hours, the cell potential for both overcharged and over-discharged batteries returned to 4 V. A measurement model analysis indicated that, after the battery was over-discharged, the battery regained the form of the impedance it had before the over-discharge excursion, suggesting that the battery reactions and dynamics were unaffected by being over-discharged. This interpretation was supported by independent measurement of battery capacity which revealed that the battery performance was not degraded by the over-discharge excursion. In contrast, the impedance of the overcharged battery continued to increase as the battery potential returned to 4 V, suggesting that the battery had suffered permanent damage. In agreement with this analysis, the measurement of battery capacity showed a decrease in performance after overcharge. The impedance of batteries at different temperatures was shown to provide a good predictor for battery performance, as indicated by cell capacity measurements at a fixed rate of charge and discharge. The battery potential was shown to provide an unreliable measure of battery health; whereas, impedance showed correctly that battery performance had been compromised by overcharging. The impedance of several batteries connected in series was shown to be sensitive to the presence of a battery that had been damaged by being overcharged. It should be noted that impedance measurements that require roughly 10 minutes were in agreement with battery capacity

measurements that, at a 1C discharge rate, required approximately 2 hours for one cycle. A second point is that impedance measurements require a small modulation of potential and are therefore much less invasive than battery capacity measurements that effectively cycle a battery from the potential at 100% state-of-charge to the potential at 0% state-of-charge. This work introduced the use of impedance superposition, guided by a measurement model analysis, to identify changes in lithium battery reactions and dynamics associated with potential excursions. The measurement model was also used to justify truncation of the high-frequency inductive feature by showing that it was inconsistent with the Kramers–Kronig relations.

Impedance spectroscopy is shown to be very sensitive to the condition and the history of the Li-ion battery. The magnitude of the impedance increased tremendously when the battery is either overcharged or over-discharged. After being overcharged, the battery returned to a potential that was well within normal potential range, but the impedance remained large. This has consequences for managing the state-of-charge of a battery stack. A battery stack is charged or discharged with whole batteries which are serially connected. Therefore, overcharge might occur for some batteries in the stack while charging. This work supports the use of impedance spectroscopy as a diagnostic tool to detect imbalances of charging conditions for individual cells in a stack.

The concept of scaled impedance was shown to be useful for correlating the impedance before and after over-discharge. The ability to superimpose scaled impedance in Nyquist plots provided evidence that the reaction chemistry was unchanged by over-discharge. The measurement model, originally developed to assess the stochastic and bias error structure of impedance data, was used to identify low and high-frequency limits of the capacitive loop needed to scale the impedance.

This work provides a guidance for the development of interpretation models for the impedance of Li-ion batteries. The influence of overcharge on the battery is envisioned to influence the low-frequency response.

The process model for impedance analysis was developed in the context of reactions and transport processes that were hypothesized to govern the performance of the battery. At the carbon electrode, lithium ions and solvent were considered to react to form a solid-electrolyte interphase (SEI). In addition, lithium ions were assumed to diffuse through the SEI to intercalate into the graphene layers. As these two processes involve an addition of currents, the corresponding impedances must be considered to be in parallel. Anomalous diffusion of lithium ions was invoked at the LiCoO2 electrode to account for the low-frequency line that was steeper than the 45 degrees predicted by ordinary diffusion. This model was fit to all impedance data collected. The model provided a good description for impedance of batteries under normal operating potentials and temperatures. The contribution of anomalous diffusion was diminished at elevated temperatures, suggesting that the free-energy well associated with anomalous or sticky diffusion was shallow. In agreement with the measurement model analysis, the model provided a good fit for the battery after the over-discharge excursion, but could not provide a good fit for the impedance of the battery after being overcharged.

This work provides an alternative explanation for the slope of the low-frequency impedance response for $LiCoO_2$ cathodes that is steeper than the 45 degrees associated with Fickian diffusion impedance. This effect is clearly associated with the unique properties of the $LiCoO_2$ cathode as the low-frequency impedance response of other Li-ion battery cathodes, e.g., $LiMn_2O_4$, $LiFePO_4$, and $Li_4Ti_5O_{12}$, show different behaviors. The group of Osaka [9] have attributed this behavior to the different time constants for diffusion to particles of different sizes, but, as other battery chemistries also have a distribution of particle sizes, their model suggests that the low-frequency impedance response for other Li-ion batteries should also differ from 45 degrees. The present work shows that anomalous diffusion may provide an explanation that is specific to the properties of $LiCoO_2$.

This work provided several new approaches for modeling the impedance of $LiCoO_2$|C batteries: the high-frequency inductive feature was truncated, following the measurement model analysis which showed that these data were inconsistent with the Kramers–Kronig relations; reactions at the graphite electrode were considered to take place in parallel; and anomalous diffusion was invoked to account for the low-frequency line that was steeper than 45 degrees. This work provides a framework for analysis of other lithium battery chemistries and, indeed, other batteries and supercapacitors.

The results presented in this work suggest several lines of research:

1. There is a need to explore the interpretation of CPE parameters in terms of capacitance for the cathode. In recent work, Orazem et al. [54] developed a model through which α and Q could be related through the capacitance to the thickness of a film. No similar model exists for the cathode within a $LiCoO_2$|C battery. It's possible that three-electrode measurements, intended to isolate the impedance of the cathode, may facilitate development of such a model.

2. The present data and that published in the literature suggest that $LiCoO_2$ possesses a property that causes a diffusion impedance that differs from that of other cathode materials. Research is needed to correlate the structure of cathode materials to impedance response. Such work may support the use of anomalous diffusion for $LiCoO_2$ cathodes and will be facilitated by new three-electrode impedance measurements that would isolate the role of the cathode.

REFERENCES

[1] M. Winter and R. J. Brodd, "What are batteries, fuel cells, and supercapacitors?," *Chem. Rev.*, vol. 104, pp. 4245–4270, 2004.

[2] K. Ozawa, ed., *Lithium Ion Rechargeable Batteries: Materials, Technology, and New Applications*. Wiley-VCH Verlag GmbH & Co., 2009.

[3] M. Kise, S. Yoshioka, K. Hamano, H. Kuriki, T. Nishimura, and H. Urushibata, "Alternating current impedance behavior and overcharge tolerance of Lithium-ion batteries using positive temperature coefficient cathodes," *Journal of The Electrochemical Society*, vol. 153, pp. A1004–A1011, 2006.

[4] G. Li, Z. Yang, and W. Yang, "Effect of $FePO_4$ coating on electrochemical and safety performance of $LiCoO_2$ as cathode material for Li-ion batteries," *Journal of Power Sources*, vol. 183, pp. 741–748, 2008.

[5] H. Maleki and J. N. Howard, "Effects of overdischarge on performance and thermal stability of a Li-ion cell," *Journal of Power Sources*, vol. 160, pp. 1395–1402, 2006.

[6] G. Chen, K. E. Thomas-Alyea, J. Newman, and T. J. Richardson, "Characterization of an electroactive polymer for overcharge protection in secondary lithium batteries," *Electrochimica Acta*, vol. 50, pp. 4666–4673, 2005.

[7] D. Belov and M.-H. Yang, "Failure mechanism of Li-ion battery at overcharge conditions," *Journal of Solid State Electrochemistry*, vol. 12, pp. 885–894, 2008.

[8] C. Love and K. Swider-Lyons, "Impedance diagnostic for overcharged Lithium-ion batteries," *Electrochemical and Solid-State Letters*, vol. 15 (4), pp. A53–A56, 2012.

[9] T. Osaka, T. Momma, D. Mukoyama, and H. Nara, "Proposal of novel equivalent circuit for electrochemical impedance analysis of commercially available Lithium ion battery," *Journal of Power Sources*, vol. 205, pp. 483 – 486, 2012.

[10] S. E. Li, B. Wang, H. Peng, and X. Hu, "An electrochemistry-based impedance model for Lithium-ion batteries," *Journal of Power Sources*, vol. 258, pp. 9–18, 2014.

[11] J. Gomez, R. Nelson, E. E. Kalu, M. H. Weatherspoon, and J. P. Zheng, "Equivalent circuit model parameters of a high-power Li-ion battery: Thermal and state of charge effects," *Journal of Power Sources*, vol. 196, pp. 4826 – 4831, 2011.

[12] M. Greenleaf, H. Li, and J. Zheng, "Application of physical electric circuit modeling to characterize Li-ion battery electrochemical processes," *Journal of Power Sources*, vol. 270, pp. 113–120, 2014.

[13] X. Hu, S. Li, and H. Peng, "A comparative study of equivalent circuit models for Li-ion batteries," *Journal of Power Sources*, vol. 198, pp. 359 – 367, 2012.

[14] M. Umeda, K. Dokko, Y. Fujita, M. Mohamedi, I. Uchida, and J. Selman, "Electrochemical impedance study of Li-ion insertion into mesocarbon microbead single particle electrode: Part i. graphitized carbon," *Electrochimica acta*, vol. 47, pp. 885–890, 2001.

[15] P. Moss, G. Au, E. Plichta, and J. Zheng, "An electrical circuit for modeling the dynamic response of Li-ion polymer batteries," *Journal of The Electrochemical Society*, vol. 155, pp. A986–A994, 2008.

[16] S. Buller, M. Thele, R. De Doncker, and E. Karden, "Impedance-based simulation models of supercapacitors and Li-ion batteries for power electronic applications," *IEEE Transactions on Industry Applications*, vol. 41, pp. 742–747, 2005.

[17] T. Dong, A. Kirchev, F. Mattera, J. Kowal, and Y. Bultel, "Dynamic modeling of Li-ion batteries using an equivalent electrical circuit," *Journal of The Electrochemical Society*, vol. 158, pp. A326–A336, 2011.

[18] T. Jacobsen and K. West, "Diffusion impedance in planar, cylindrical and spherical symmetry," *Electrochimica acta*, vol. 40, pp. 255–262, 1995.

[19] J. Huang, H. Ge, Z. Li, and J. Zhang, "An agglomerate model for the impedance of secondary particle in Lithium-ion battery electrode," *Journal of The Electrochemical Society*, vol. 161, pp. E3202–E3215, 2014.

[20] P. Albertus, J. Christensen, and J. Newman, "Experiments on and modeling of positive electrodes with multiple active materials for Lithium-ion batteries," *Journal of the Electrochemical Society*, vol. 156, pp. A606–A618, 2009.

[21] J. M. Tarascon and M. Armand, "Issues and challenges facing rechargeable lithium batteries," *Nature*, vol. 414, pp. 359–367, 2001.

[22] G. Pistoia, "Chapter 1 - nonaqueous batteries used in industrial applications," in *Industrial Applications of Batteries* (M. Broussely and G. Pistoia, eds.), pp. 1 – 52, Amsterdam: Elsevier, 2007.

[23] J. B. Goodenough, H. D. Abruña, and M. V. Buchanan, eds., *Basic Research Needs for Electrical Energy Storage: Report of the Basic Energy Sciences Workshop on Electrical Energy Storage, April 2-4, 2007.* Washington, DC: Office of Basic Energy Sciences, Department of Energy, 2007.

[24] D. Linden and T. B. Reddy, *Handbook of Batteries.* McGraw-Hill, 2002.

[25] C. Mikolajczak, *Lithium-ion Batteries Hazard and Use Assessment.* New York: Springer, 2011.

[26] H. D. Abruña, Y. Kiya, and J. C. Henderson, "Batteries and electrochemical capacitors," *Physics Today*, vol. 61, pp. 43–47, 2008.

[27] M. E. Orazem and B. Tribollet, *Electrochemical Impedance Spectroscopy*. Hoboken, NJ: John Wiley & Sons, 2008.

[28] "Rechargeable Li-ion button battery serial LIR2032." http://www.batteryspace.com/productimages/aa/20060224/LIR2032_new1.pdf. Accessed: 03-08-2014.

[29] P. Ramadass, B. Haran, R. White, and B. N. Popov, "Performance study of commercial $LiCoO_2$ and spinel-based Li-ion cells," *Journal of Power Sources*, vol. 111, pp. 210–220, 2002.

[30] S. Tintignac, R. Baddour-Hadjeana, J.-P. Pereira-Ramosa, and R. Salotb, "High performance sputtered $LiCoO_2$ thin films obtained at a moderate annealing treatment combined to a bias effect," *Electrochimica Acta*, vol. 60, pp. 121–129, 2012.

[31] S. Watanabe, M. Kinoshita, and K. Nakura, "Capacity fade of $LiNi_{(1-x-y)}Co_xAl_yO_2$ cathode for Lithium-ion batteries during accelerated calendar and cycle life test. i. comparison analysis between $LiNi_{(1-x-y)}Co_xAl_yO_2$ and $LiCoO_2$ cathodes in cylindrical Lithium-ion cells during long term storage test," *Journal of Power Sources*, vol. 247, pp. 412–422, 2014.

[32] S. Erol, "Electrochemical impedance analysis of lithium cobalt oxide batteries," Master's thesis, University of Florida, 2011.

[33] "Powerstream Li-ion coin cell Lir2032 data sheet." http://www.powerstream.com/p/Lir2032.pdf. Accessed: 03-08-2014.

[34] B. Hirschorn, B. Tribollet, and M. E. Orazem, "On selection of the perturbation amplitude required to avoid nonlinear effects in impedance measurements," *Israel Journal of Chemistry*, vol. 48, pp. 133–142, 2008.

[35] S. Erol, M. E. Orazem, and R. P. Muller, "Influence of overcharge and over-discharge on the impedance response of $LiCoO_2$|C batteries," *Journal of Power Sources*, vol. 270, pp. 92 – 100, 2014.

[36] E. Buiel and J. Dahn, "Li-insertion in hard carbon anode materials for Li-ion batteries," *Electrochimica Acta*, vol. 45, pp. 121 – 130, 1999.

[37] M. E. Orazem, "A systematic approach toward error structure identification for impedance spectroscopy," *Journal of Electroanalytical Chemistry*, vol. 572, pp. 317–327, 2004.

[38] P. Agarwal, M. E. Orazem, and L. H. García-Rubio, "Measurement models for electrochemical impedance spectroscopy: I. demonstration of applicability," *Journal of The Electrochemical Society*, vol. 139, pp. 1917–1927, July 1992.

[39] P. Agarwal, O. D. Crisalle, M. E. Orazem, and L. H. García-Rubio, "Measurement models for electrochemical impedance spectroscopy: 2. determination of the stochastic contribution to the error structure," *Journal of The Electrochemical Society*, vol. 142, pp. 4149–4158, 1995.

[40] P. Agarwal, M. E. Orazem, and L. H. García-Rubio, "Measurement models for electrochemical impedance spectroscopy: 3. evaluation of consistency with the kramers-kronig relations," *Journal of The Electrochemical Society*, vol. 142, pp. 4159–4168, 1995.

[41] P. Agarwal, M. E. Orazem, and L. H. García-Rubio, "Application of the kramers kronig relations to electrochemical impedance spectroscopy," in *Electrochemical Impedance: Analysis and Interpretation* (J. Scully, D. Silverman, and M. Kendig, eds.), vol. ASTM STP 1188, (Philadelphia, PA), pp. 115–139, American Society for Testing and Materials, 1993.

[42] G. Baril, G. Galicia, C. Deslouis, N. Pèbére, B. Tribollet, and V. Vivier, "An impedance investigation of the mechanism of pure magnesium corrosion in sodium sulfate solutions," *Journal of The Electrochemical Society*, vol. 154, pp. C108–C113, 2007.

[43] M. E. Orazem, P. T. Wojcik, M. Durbha, I. Frateur, and L. H. García-Rubio, "Application of measurement models for interpretation of impedance spectra for corrosion," *Mat. Sci. Forum*, vol. 289-292, pp. 813–828, 1998.

[44] G. G. Amatucci, J. M. Tarascon, and L. C. Klein, "CoO_2, the end member of the $LiCoO_2$ solid solution," *Journal of The Electrochemical Society*, vol. 143, pp. 1114–1123, 1996.

[45] M. B. Pinson and M. Z. Bazant, "Theory of SEI formation in rechargeable batteries: Capacity fade, accelerated aging and lifetime prediction," *Journal of The Electrochemical Society*, vol. 160, pp. A243–A250, 2013.

[46] J. Christensen and J. Newman, "A mathematical model for the Lithium-ion negative electrode solid electrolyte interphase," *Journal of The Electrochemical Society*, vol. 151, pp. A1977–A1988, 2004.

[47] R. Deshpande, M. Verbrugge, Y.-T. Cheng, J. Wang, and P. Liu, "Battery cycle life prediction with coupled chemical degradation and fatigue mechanics," *Journal of The Electrochemical Society*, vol. 159, pp. A1730–A1738, 2012.

[48] D. Aurbach, B. Markovsky, I. Weissman, E. Levi, and Y. Ein-Eli, "On the correlation between surface chemistry and performance of graphite negative electrodes for Li ion batteries," *Electrochimica acta*, vol. 45, pp. 67–86, 1999.

[49] J. Thevenin, "Passivating films on lithium electrodes. an approach by means of electrode impedance spectroscopy," *Journal of Power Sources*, vol. 14, 1985.

[50] J. Song and M. Z. Bazant, "Effects of nanoparticle geometry and size distribution on diffusion impedance of battery electrodes," *Journal of The Electrochemical Society*, vol. 160, pp. A15–A24, 2013.

[51] J.-Y. Go and S.-I. Pyun, "A review of anomalous diffusion phenomena at fractal interface for diffusion-controlled and non-diffusion-controlled transfer processes," *Journal of Solid State Electrochemistry*, vol. 11, pp. 323–334, 2007.

[52] J. F. Lutsko and J. P. Boon, "Microscopic theory of anomalous diffusion based on particle interactions," *Physical Review E*, vol. 88, p. 022108, 2013.

[53] J. Bisquert and A. Compte, "Theory of the electrochemical impedance of anomalous diffusion," *Journal of Electroanalytical Chemistry*, vol. 499, pp. 112 – 120, 2001.

[54] M. E. Orazem, I. Frateur, B. Tribollet, V. Vivier, S. Marcelin, N. Pébère, A. L. Bunge, E. A. White, D. P. Riemer, and M. Musiani, "Dielectric properties of materials showing constant-phase-element (CPE) impedance response," *Journal of The Electrochemical Society*, vol. 160, pp. C215–C225, 2013.

BIOGRAPHICAL SKETCH

Salim Erol received his Bachelor of Science degree in chemical engineering from Eskisehir Osmangazi University in June of 2006. Then he began a master's program at Marmara University in Turkey. While he was preparing his master's thesis, he applied for a government scholarship, and he was chosen as a scholar for his masters. Consequently, he had to leave his program in Turkey, in order to make a new start toward a master's degree and Ph.D. from an American university. To reach a sufficient level in English, he studied at an English-language school, the English Programs for Internationals at the University of South Carolina, and finished the school in April of 2009. After, he entered the University of Florida as a master's student in the chemical engineering department in August of 2009. He got his master's degree in August of 2011. He has been in the electrochemical impedance research group as a research assistant, under the direction of Professor Mark E. Orazem, since January of 2010.